Monitoring and Prediction of Porosity in Laser Powder Bed Fusion using Physics-informed Meltpool Signatures and Machine Learning

Ziyad Smoqi[1*], Aniruddha Gaikwad[1], Benjamin Bevans[1], Md Humaun Kobir[1], James Craig[2], Alan Abul-Haj[3], Alonso Peralta[4], Prahalada Rao[1]

[1]University of Nebraska-Lincoln; [2]Stratonics; [3]ARA Engineering; [4]Honeywell

*Corresponding author, email: zsmoqi@huskers.unl.edu

Abstract

In this work we accomplished the monitoring and prediction of porosity in laser powder bed fusion (LPBF) additive manufacturing process. This objective was realized by extracting physics-informed meltpool signatures from an in-situ dual-wavelength imaging pyrometer, and subsequently, analyzing these signatures via computationally tractable machine learning approaches. Porosity in LPBF occurs despite extensive optimization of processing conditions due to stochastic causes. Hence, it is essential to continually monitor the process with in-situ sensors for detecting and mitigating incipient pore formation. In this work a tall cuboid-shaped part (10 mm × 10 mm × 137 mm, material ATI 718Plus) was built with controlled porosity by varying laser power and scanning speed. This test caused various types of porosity, such as lack-of-fusion and keyhole formation, with varying degrees of severity in the part. The meltpool was continuously monitored using a dual-wavelength imaging pyrometer installed in the machine. Physically intuitive process signatures, such as meltpool length, temperature distribution, and ejecta (spatter) characteristics, were extracted from the meltpool images. Subsequently, relatively simple machine learning models, e.g., K-Nearest Neighbors, were trained to predict both the severity and type of porosity as a function of these physics-informed meltpool signatures. These models resulted in a prediction accuracy exceeding 95% (statistical F1-score). The same analysis was carried out with a complex, black-box deep learning convolutional neural network which directly used the meltpool images instead of physics-informed features. The convolutional neural network produced a comparable F1-score in the range of 89% to 97%. These results demonstrate that using pragmatic, physics-informed meltpool signatures within a simple machine learning model is as effective for flaw prediction in LPBF as using a complex and computationally demanding black-box deep learning model.

Keywords: Laser Powder Bed Fusion; Porosity Prediction; Meltpool Monitoring; Imaging Pyrometer; Physics-Informed Machine Learning.

1 Introduction

1.1 Motivation and Objective

In laser powder bed fusion (LPBF) additive manufacturing, energy from a laser beam is used to selectively fuse powder particles to produce three-dimensional objects in a layer-by-layer manner (Sames et al., 2016). A schematic representation of the LPBF process is shown in Figure 1. The process can produce geometries which are difficult, if not impossible, to make using traditional subtractive and formative processes (Druzgalski et al., 2020). Despite the potential of LPBF to overcome the material and design barriers of traditional manufacturing, safety-critical industries such as aerospace are reticent in adopting the process due to the lack of part consistency and tendency of the process to create flaws (Grasso and Colosimo, 2019). This uncertainty in part quality leads to large variation in functional properties (Yadollahi and Shamsaei, 2017).

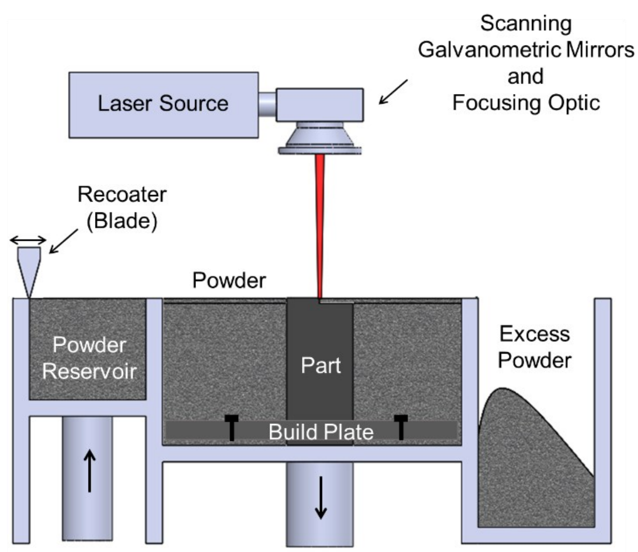

Figure 1: Schematic representation of the laser powder bed fusion (LPBF) additive manufacturing process.

Some of the quality-related challenges in LPBF include porosity, microstructure inhomogeneity, cracking, etc., that result from substandard powder feedstock, improper selection of the process parameters, and unsuitable design of the part (Guo et al., 2020). Optimizing process parameters to minimize flaw formation via empirical design of experiments is both expensive and time consuming

(Megahed et al., 2019). Further, an experimentally derived processing window may not transfer to different parts built with the same material and using the same equipment because flaw formation in LPBF depends on part design, build orientation, presence of support structures, among others (Yavari et al., 2021b). Moreover, despite extensive process optimization, flaw formation in LPBF is liable to occur on account of stochastic (chance-related) factors, such as presence of ejecta (spatter) from the process (Schwerz et al., 2021). Hence, in-process monitoring of build quality using data acquired from in-situ sensors is a critical and urgent need in LPBF (Mani et al., 2017).

The objective of this work is to detect and predict the type and the severity of porosity in a LPBF part using in-process meltpool signatures acquired from an imaging pyrometer. This is an important area of research, because, porosity can significantly degrade the functional properties of the part, such as its fatigue life, and compromise its structural integrity (Lewandowski and Seifi, 2016). To explain further, the meltpool is the region where the laser melts the powder to create a dynamic volume of molten material, typically 50 to 100 μm in depth or width, and close to one millimeter in length (Lane et al., 2020a). The complex thermal and fluid flow phenomena of the meltpool influences the microstructure evolved and flaw formation, including porosity, in LPBF (Oliveira et al., 2020b). Although quality benchmarks in LPBF are in their early stages (Ronneberg et al., 2020), as an industry consensus, LPBF-processed parts are expected to exceed 99% of the theoretical density of the material to be considered functionally deployable (Kamath et al., 2014). In this work, physics-informed features are extracted from the meltpool images based on theoretical simulations and experimental observations reported in the literature (Khairallah et al., 2016). These features are subsequently used to predict the type and severity of pore formation via relatively simple, readily implemented and computationally tractable machine learning models, such as K-Nearest Neighbors. The underlying hypothesis is that a small set of pragmatic, physics-informed features extracted from meltpool data when used with simple machine learning models will detect part flaws at par with a complex and computationally intensive deep machine learning model that uses raw meltpool images (Du et al., 2021).

From a practical perspective, it is important to detect both the severity (amount) of porosity and its nature (type) to aid process correction (Seifi et al., 2016). This is not only an active research area in LPBF, but also in other AM processes, such as wire and arc AM (Ramalho et al., 2022). To explain further, in LPBF, and metal-based AM processes in general, the type of porosity can be classified into three broad categories contingent on the causal process phenomena, these are: (i) lack-of-fusion, (ii) keyhole formation, and (iii) gas porosity (Snow et al., 2020). Lack-of-fusion pores are characterized by their irregular (acicular) shape and are caused by partial fusion of powder material on account of insufficient input energy. In contrast to lack-of-fusion porosity, keyhole pores are caused by vaporization of material due to excessive input energy and are typically circular in appearance (DebRoy et al., 2018). The third category of porosity called gas porosity, is typified by circular shaped pores which can result either from voids present in the feedstock material, or gasses escaping from the meltpool (Snow et al., 2020). Given their large size and irregular size, lack-of-fusion pores are comparatively more detrimental to functional integrity (Gorelik, 2017). In this work, only lack-of-fusion and keyhole porosity were observed.

1.2 Previous Work and Novelty

In-process monitoring in LPBF is an area of active research. Several recent review articles have detailed the various sensing modalities and data-driven monitoring approaches that are currently being investigated. We point the reader to articles by Lane et al. (2020b), Everton et al. (2016), Spears and Gold (2016), and Grasso and Colosimo (2017), which provide comprehensive review of the state-of-the-art in sensing and process monitoring in LPBF. Likewise, the application of machine learning for process monitoring in LPBF has been recently reviewed by Mozaffar et al. (2022), Wang et al. (2020), Meng et al. (2020), and Razvi et al. (2019). Herewith we review a few representative papers from the literature.

In previous work reported in the literature, the characteristics of meltpool region has been extensively used for monitoring build quality (Li et al., 2022). For example, Felix et al. (2021) used a multiple sensor setup including a photodiode and an optical camera to predict shift in process conditions at two levels, i.e., increase in laser power and decrease in scanning speed by 10%. Furthermore, the authors predicted the occurrence of defects (porosity and cracking) due to these process drifts. For these prediction tasks, the authors proposed a novel Bayesian approach along with least squares regression models that yielded prediction fidelity (R^2) of up to 92%. Similarly, Clijsters et al. (2014) proposed an in-situ monitoring system equipped with two optical sensors (a photodiode and an IR camera), allowing the LPBF operator to log and analyze meltpool data. A high correlation between the in-situ meltpool signatures and offline porosity analysis was reported by Clijsters et al. (2014) thus providing an opportunity for future closed-loop process control. Scime and Beuth (2019) used an off-axis high-speed imaging camera to obtain in-situ images of the meltpool and trained a support vector machine (SVM) model to correlate meltpool signatures with porosity. Likewise, Kwon et al. (2020) used meltpool images acquired via a high speed camera and classified the images using a deep learning neural network to show the potential of the approach for in-situ defect detection. Recently, Forien et al. (2020) combined data from a high-speed infrared diode-based pyrometer and a high-speed imaging camera for in-situ monitoring of defects in LPBF processed single track constructs.

Apart from meltpool characteristics, several studies have also correlated plume and spatter formation with the part quality (Snow et al., 2020). Plume forms due to the ionization of metal vapor released from the meltpool, while spatter refers to the semi-solid droplets that escape from the meltpool on account of the recoil pressure (Wang et al., 2020) or partially melted particles entrained by the vapor jet (Ly et al., 2017). In this context, Zhang et al. (2018) used an off-axis high speed camera for monitoring an LPBF process and observed that combining features from the plume, spatter and meltpool improved the ability of a SVM model to predict the quality (continuity and width) of single tracks made using LPBF. Additionally, the authors employed a complex, deep learning neural network using raw images to make these predictions and observed a better classification performance compared to SVM. Similarly, Ye et al. (2018) and Tan et al. (2020) used deep learning neural networks to correlate plume and spatter formation with the build quality.

More recently, Snow et al. (2022) used in-situ sensor data, including layer-wise images, multi-spectra emission and laser scan vector data, for process monitoring in LPBF. The author correlated the in-situ acquired data to lack-of-fusion defects identified via XCT. Further, they trained convolutional neural networks (CNN) to differentiate nominal build conditions from those leading to flaw formation. The trained network was applied to an independent build and yielded defect detection with a high accuracy (>93%), which suggests the high likelihood of real-time flaw detection using this approach. Ultimately, the results from machine learning were correlated with the fatigue properties of the parts as lack-of-fusion defects are considered fatigue critical defects (Snow et al., 2022).

Thus, researchers in the previous works have used in-situ monitoring of plume and spatter signatures, meltpool shape and intensity and layer-wise images using various sensors to qualify the build quality in LPBF (Wang et al., 2020). However, a drawback in these previous studies is that the sensor signatures are correlated to flaw formation using complex machine learning techniques such as deep learning convolutional neural networks. Such deep learning techniques lack physical interpretability and are hard to generalize beyond specific situations (Gaikwad et al., 2019). Moreover, such complex machine learning models require high-end graphical processing units to train and deploy given their computationally demanding nature. Hence, the data acquired must be transferred from the sensors to a separate, dedicated computation unit. The storage and transfer of this high volume of in-process data for analysis introduces a latency in process monitoring. Consequently, there is a need for computationally tractable monitoring approaches that eliminate the need to transfer memory-intensive sensor data to a dedicated analysis engine. To overcome these challenges with black-box machine learning approaches, researchers have recently embarked on combining fundamental understanding of the process physics to aid machine learning models in flaw detection. Efforts towards such a physics-informed machine learning approach to aid process monitoring in additive manufacturing is evident in recent articles by Ness et al. (2022), Guo et al. (2022), Du et al. (2021), and Yavari et al. (2021a).

The novelty of this work lies in extracting only four physically intuitive meltpool features, such as meltpool shape and temperature, from an imaging pyrometer and consequently using these features to predict porosity via simple machine learning models. Such a physics-aided approach to a flaw monitoring and detection in LPBF is shown to have the following advantages:

(1) The low-level meltpool temperature and shape features used in this work are physically intuitive and relatively tractable to extract. Their interpretability and ease of computation aids rapid training of models with smaller data sets, and potentially facilitates transferability across different materials and machines.
(2) Computationally tractable machine learning approaches can be used to predict flaw formation instead of complex deep learning algorithms. Consequently, the large volume of meltpool data can be analyzed on the edge, i.e., on-board the LPBF machine, without the need to transfer data away from the machine to a separate analysis engine. Such near-the-edge computation facilitates rapid process feedback correction.

The rest of this paper is organized as follows. Sec. 2 details the methodology, encompassing the experimental setup, creation of test coupons, characterization of samples, extraction of meltpool signatures from the pyrometry data, and their subsequent use in machine learning for prediction of porosity. Sec. 3 describes the results, including elucidation of the physical link between meltpool signatures and porosity and prediction of the type and severity of porosity. Conclusion and avenues for future work are summarized in Sec. 4.

2 Methods

2.1 Experimental Setup

Experiments were conducted on an EOS M280 LPBF system that utilizes a continuous mode ytterbium-fiber laser (wavelength 1070 nm), which has a Gaussian distribution with a spot size of 100 μm ($1/\varepsilon^2$). The system was integrated with a dual wavelength imaging pyrometer (Stratonics, ThermaViz) to acquire meltpool images. A schematic of this apparatus is shown in Figure 2(a). The pyrometer was in an off-axis configuration, and was inclined at 81° to the horizontal as illustrated in Figure 2(a). The meltpool images were acquired at a sampling rate of 800 Hz and resolution of 370 × 384 pixels (29 μm per pixel spatial resolution). The sensor images approximately 120 mm^2 in the center of the part. A sample meltpool image is exemplified in Figure 2(b). The change in the meltpool behavior as a function of process conditions is summarized later in Sec. 2.4.

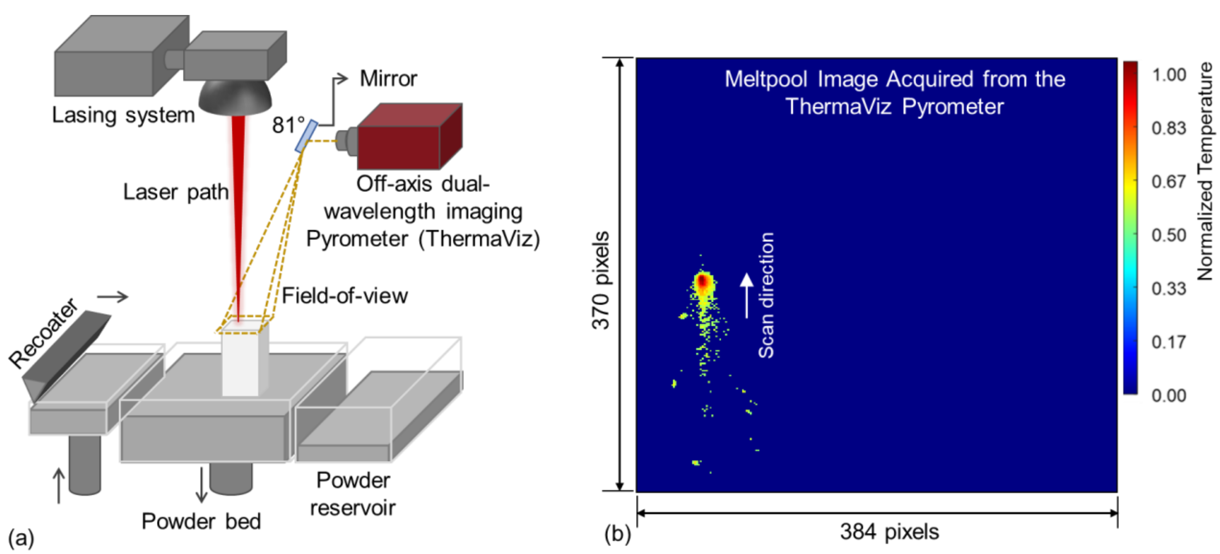

Figure 2: Schematic representation of the experimental setup showing (a) the off-axis dual wavelength imaging pyrometer (Stratonics, ThermaViz) and (b) a sample meltpool image and temperature field acquired by the pyrometer at 800 Hz sampling rate and 29 μm/pixel resolution.

The working principle of the pyrometry is governed by Planck's law, which states that the intensity (I_λ) of radiation from a heated object is proportional to the object's temperature (T_λ) at a particular wavelength (λ), i.e. $I_\lambda = \epsilon \, T_\lambda$ (Hooper, 2018). The constant of proportionality (ϵ) is the thermal emissivity of the object. However, in practice the thermal emissivity of an object is not constant and is dependent on several factors such as the temperature of the object, surface characteristics, and the inclination of the sensor to the surface at which the temperature is measured (Moylan et al., 2014). To mitigate the effect of change in thermal emissivity as a function of temperature, the dual-wavelength imaging pyrometer in this work measures the intensity of radiation at two wavelengths ($\lambda_1 = 720$ nm and $\lambda_2 = 900$ nm). The key idea is to estimate the temperature of the body as a function of ratio of the intensity radiation at two different wavelengths. Taking the ratio of intensities at two different wavelengths, ($\frac{I_{\lambda 1}}{I_{\lambda 2}}$) has the effect of canceling out the emissivity term. Hence, the temperature measurement obtained by the dual-wavelength imaging pyrometer used in this work is a close approximation of the absolute meltpool temperature and is more accurate than the temperature measurement obtained by a single-wavelength pyrometer or an infrared thermal camera (Wang et al., 2007). The pyrometer was calibrated using the industry-standard black-body measurement approach (Mitchell et al., 2020). The accuracy of temperature measurement using a pyrometer, albeit instrument dependent, is typically within ±5°C (Everton et al., 2016). To ensure generalizability to different materials, and as a standard practice in machine learning, the meltpool temperatures in this work are normalized between 0 and 1.

2.2 Experiments

A large cuboid (10 mm × 10 mm × 137 mm, Figure 3) was built with varying processing conditions contingent on the build height. The material used in this experiment was ATI 718Plus alloy powder with a particle size in the range of 10 – 60 μm. The chemical composition of the powder is shown in Table 1. The ATI 718Plus alloy is a modified version of Inconel 718, in which Co is replaced with ½ of its Fe-content, 1wt.% W is added, and Al/Ti ratio is increased (Kennedy, 2005). This modification increases the service temperature of the ATI 718Plus alloy and improves its mechanical properties (Kennedy, 2005).

Table 1: Nominal chemical composition (wt. %) of ATI 718Plus alloy.

Alloy	Chemical Composition (wt.%)									
	Ni	Cr	Fe	Co	Nb	Mo	Al	W	Ti	C
ATI 718Plus Powder	Balance	17.7	9.59	9.19	5.62	2.51	1.58	1.00	0.78	0.020

During the build, two process parameters were varied, namely laser power (P) and scanning speed (V) at different build heights. Figure 3 and Table 2 summarize these experimental conditions. The intent is to create different types of porosity (lack-of-fusion and keyhole) with varying level of severity. Previous work has shown that the laser power (P) and scanning speed (V), along with the layer height (T) and hatch spacing (H) are the most consequential to flaw formation (du Plessis, 2019). The effect of varying these parameters on the type and severity of porosity is elucidated in depth in Sec. 3.1 and Sec. 3.2, respectively. The rationale for building one tall test part instead of several small coupons as commonly done in the literature (Montazeri et al., 2020), is as follows. In LPBF the location of the part on the build plate is known to have a significant effect on part quality (Foster et al., 2015). Hence, to mitigate the effect of part location, instead of processing several small samples each under a different process condition, in this work, we built one part with processing conditions changed at different layers, as demarcated in Figure 3.

Referring to Figure 3 and Table 2, the build was started with a nominal condition, labeled P0, and processed with laser power (P) 300 W, and scanning speed (V) 1650 mm·s^{-1}. These nominal conditions were recommended by the powder supplier (ATI) based on empirical studies. The processing continued under nominal conditions for 25 mm (layer 0 – 833). For the entirety of the experiment, the layer thickness (T) was fixed at 30 µm and a rectilinear scanning strategy with 90° shift between successive layers was followed.

The next 25 mm (layer 833 – 1667) of the part, labeled P1-P5, was built with laser power (P) varying from 120 W to 325 W with scanning speed (V) fixed at 1650 mm·s^{-1}. We note that P2 is identical to the nominal condition (P0). From 50 mm (layer 1667) to 75 mm (layer 2500), labeled S1-S5, the laser power

(P) was fixed at 370 W, the scanning speed (V) was varied from 880 mm·s^{-1} to 3780 mm·s^{-1}, and the hatch spacing (H) was increased from 0.09 mm for P0-P5 to 0.14 mm for S1-S5. The rest of the part was built with variation of contour patterns, the effects of which are not studied in this work.

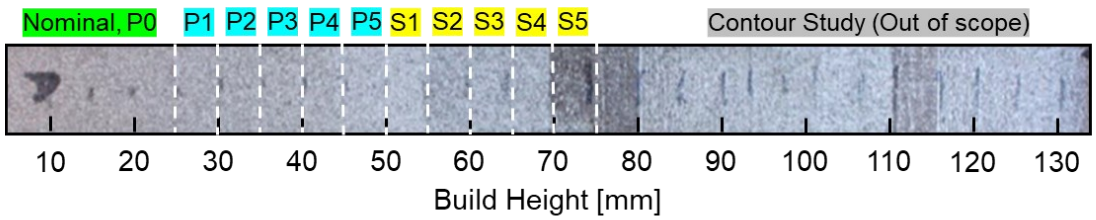

Figure 3: Photograph of as-build ATI 718Plus part, demarcating segments produced under different processing parameters (reported in Table 2). The part is 10 mm × 10 mm ×137 mm (build height), consisting of 4567 individual layers of 30 µm layer height.

Table 2: Process parameters used for LPBF experiments used in this work.

<table>
<tr><th colspan="2">Process Step</th><th>Laser Power
P [W]</th><th>Scanning Speed
V [mm·s−1]</th><th>Hatch Spacing
H [mm]</th><th>Build Height
T [mm]</th><th>Layer Number</th></tr>
<tr><td colspan="2">Nominal, P0</td><td>300</td><td>1650</td><td>0.09</td><td>0 – 25</td><td>1-833</td></tr>
<tr><td rowspan="5">Variation in Laser Power</td><td>P1</td><td>325</td><td rowspan="5">1650</td><td rowspan="5">0.09</td><td>25 – 30</td><td>833-1000</td></tr>
<tr><td>P2</td><td>300</td><td>30 – 35</td><td>1000-1167</td></tr>
<tr><td>P3</td><td>275</td><td>35 – 40</td><td>1167-1333</td></tr>
<tr><td>P4</td><td>180</td><td>40 – 45</td><td>1333-1500</td></tr>
<tr><td>P5</td><td>120</td><td>45 – 50</td><td>1500-1667</td></tr>
<tr><td rowspan="5">Variation in Scanning Speed</td><td>S1</td><td rowspan="5">370</td><td>3780</td><td rowspan="5">0.14</td><td>50 – 55</td><td>1667-1833</td></tr>
<tr><td>S2</td><td>3000</td><td>55 – 60</td><td>1833-2000</td></tr>
<tr><td>S3</td><td>2200</td><td>60 – 65</td><td>2000-2167</td></tr>
<tr><td>S4</td><td>1320</td><td>65 – 70</td><td>2167-2333</td></tr>
<tr><td>S5</td><td>880</td><td>70 – 75</td><td>2333-2500</td></tr>
</table>

2.3 Porosity Characterization and Measurement

After processing, the part was detached from the build plate using wire electro-discharge machining. Subsequently, the severity of porosity was quantified using non-destructive X-ray computed tomography (XCT, Nikon XTH 225 ST). The entire part was scanned at a voxel resolution of 15 μm and the resulting XCT image slices were analyzed using the Volume Graphics software (VGSTUDIOMAX 3.3.4) native to the XCT machine. The level of porosity is reported in terms of defect volume ratio (DVR) – a commonly used metric in the literature to quantify porosity (Wells, 2007); DVR is defined as,

$$DVR[\%] = \frac{\sum_{i=1}^{n} v_i}{V_P} \times 100, \tag{1}$$

where n is the total number of voxels belongs to porosity in a part, v_i is a single voxel belong to a pore detected by the XCT software, and V_P is the total volume of the part in voxels. We note that the voxel resolution of 15 μm used for the XCT analysis, limits the minimum pore size that can be reliably detected to 30 μm. Apart from XCT, we measured the relative density of each segment corresponding to the changes in laser power (P0 – P5) and scanning speed (S1 – S5) using the Archimedes method (Slotwinski and Garboczi, 2014).

The type of porosity was investigated using optical microscopy and scanning electron microscopy (Jeol JCM-6000 Plus). Sample preparation for microscopy analysis included further sectioning of the part into smaller samples of 10 mm × 10 mm × 5 mm along the vertical height corresponding to the processing segments (P1 – P5, S1 – S5) reported in Table 2 and Figure 3. Next, the samples for each the ten processing conditions (P1-P5, S1-S5) were further cross-sectioned into two smaller sections for characterization along the XY-plane (normal to the build direction) and XZ-plane (parallel to the build direction). The resulting 20 samples after cross-sectioning were embedded in resin, progressively ground with finer silicon carbide abrasive pads, and polished using diamond paste (3, 1, 0.5 μm) to a mirror finish. After polishing, the samples were etched by swabbing the surface with aqua regia (HCL: HNO_3, 3:1) for approximately ten seconds.

2.4 Representative Sensor Data

Shown in Figure 4 are representative examples of the meltpool images acquired from the pyrometer under various laser power (P) and scanning speed (V) conditions. The top row of Figure 4 shows representative meltpool images acquired while varying the laser power over the segments (P1 – P5). Over the segments (P1 – P5), which are 5 mm tall and separated along the build height, the laser power was reduced from 325 W – 120 W while the scanning speed was fixed at V = 1650 mm·s^{-1}.

In Figure 4, the power (P), scanning speed (V), layer thickness (T) and hatch spacing (H) are combined into the volumetric energy density (E_v, J·mm^{-3}) which is expressed as follows.

$$E_v = \frac{P}{T \cdot V \cdot H} \tag{2}$$

Visual examination of the meltpool images obtained by the imaging pyrometer (Figure 4) indicates that the meltpool size and shape are related to the processing conditions. For example, referring to the top row of Figure 4, the meltpool size and shape remain consistent when the laser power was reduced over the segments (P1 – P4) from 325 W to180 W. Likewise, the temperature distribution of the meltpool and ejecta also remained consistent as the laser power was reduced from 325 W to 180 W. However, when the laser power was further reduced to 120 W (segment P5), the spatter becomes prominent and relatively hotter ejecta particles were observed in the areas further away from the core meltpool region.

The bottom row of Figure 4 shows representative meltpool images acquired while varying the scanning speed over the segments (S1 – S5), wherein the scanning speed was reduced from 3780 mm·s^{-1} to 880 mm·s^{-1} and the laser power was fixed at P = 370 W. For the high scanning speed conditions (V > 2200 mm·s^{-1}) compared to laser power conditions (P1 – P4), the meltpool is relatively elongated and the ejecta travels further from the meltpool. Likewise, the meltpool images from the higher scanning speed conditions (V > 2200 mm·s^{-1}) depict hotter ejecta particles when compared with those from the lower scanning speed conditions ($V \leq$ 2200 mm·s^{-1}). These observations provided the bases for extracting meltpool shape and temperature features and correlating these features to porosity type and severity.

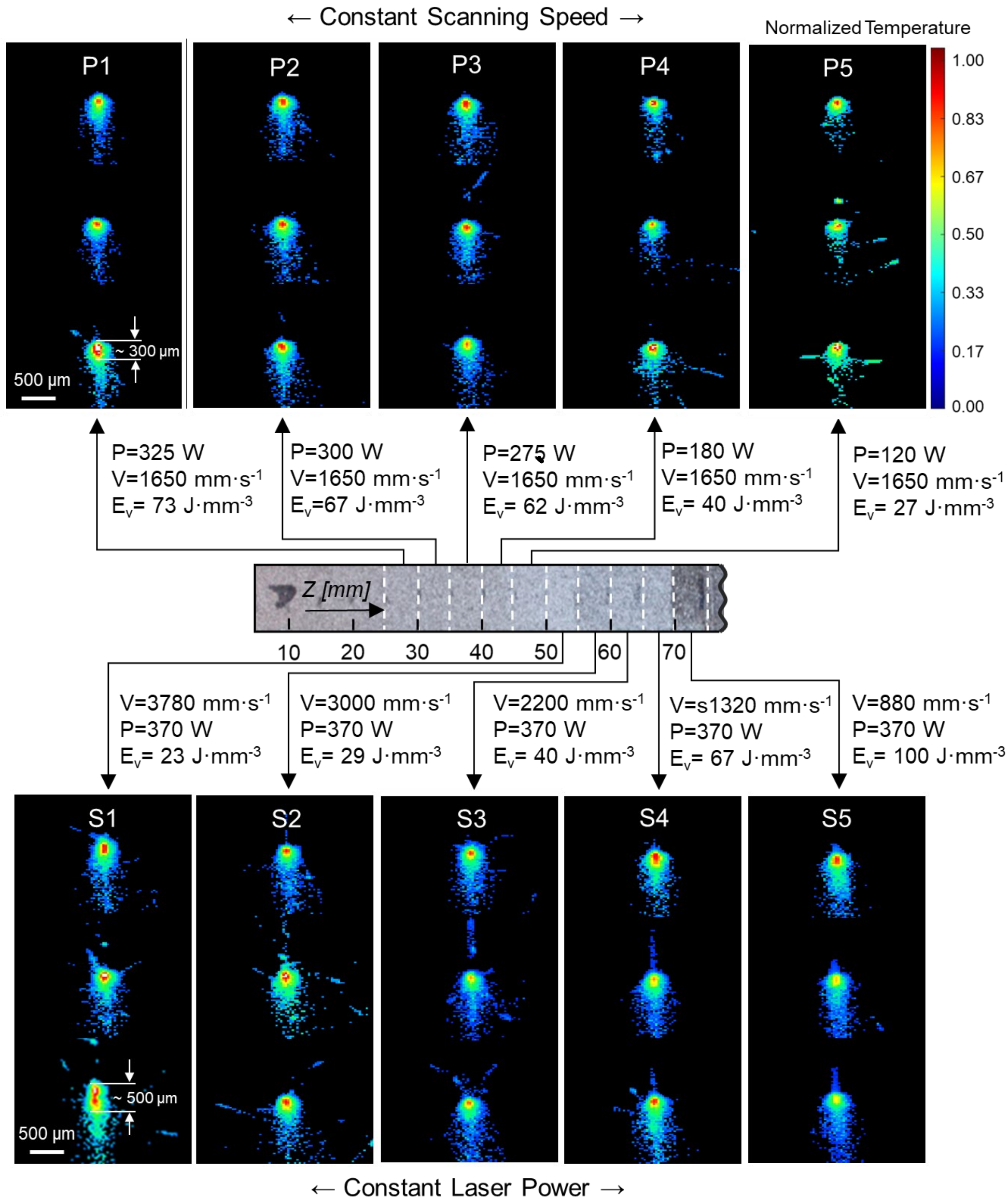

Figure 4: Representative meltpool images acquired in-situ using the imaging pyrometer for the build segments printed with varying laser power (top row) and scanning speed (bottom row). The meltpool shape and spatter characteristics change significantly with the processing conditions. For example, comparing P1 and S1, the large increase in scanning speed at S1 (3780 mm·s^{-1}) compared to P1 (1650 mm·s^{-1}) results in prominent spatter.

2.5 Processing of Pyrometer Data and Feature Extraction

To extract meltpool signatures, we first separated the ejecta (spatter and meltpool tail) from the body of the meltpool. The meltpool body was defined as a 40 pixel $\times$ 40 pixel area with its center coincident with the hottest pixel in the meltpool as shown in Figure 5(a). At this spatial resolution, the meltpool body was ~1160 μm$\times$1160 μm. The rest of the image was considered part of the ejecta.

The meltpool body was further processed using K-means image segmentation (Gaikwad et al., 2020). This approach was used to segment the meltpool body into 3 clusters based on the image intensity. Then the cluster belonging to the hottest region of the meltpool was considered as the final meltpool image as shown in Figure 5(b). We note that K-means image segmentation is readily implemented through a pre-existing function in MATLAB.

From the pyrometer images in Figure 5, physically intuitive meltpool and spatter morphology (shape) and temperature distribution signatures were extracted. Figure 5(b) and (c) are representative meltpool and ejecta images, respectively, for temperature-based signatures, while Figure 5(d) and (e) are the corresponding binarized (black-and-white) images used for morphology-based signatures. For morphology- or shape-based features, the Euclidean distance from the center of the meltpool to edge pixels and ejecta pixels was used (indicated by red arrows shown in Figure 5(d) and (e)). For temperature-based features, the normalized temperature values of all pixels belonging to the meltpool, and ejecta were computed. The meltpool temperature was normalized between 0 to 1 to aid machine learning models and facilitate generalizability of the approach across different materials in the future.

A total of four physics-informed meltpool and ejecta features were devised to capture the meltpool characteristics for each segment representative of a different processing condition. The rationale for selection of these features based on literature and the approach to estimate these from the pyrometer images are described herewith.

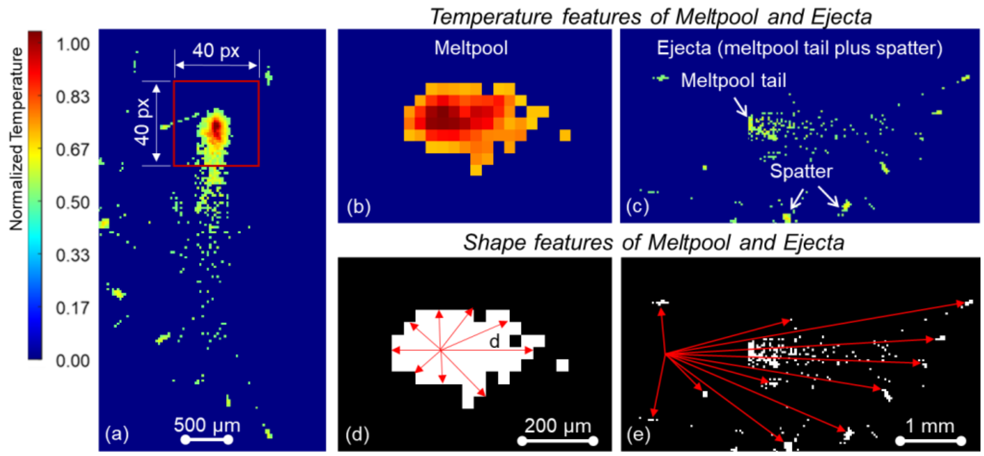

Figure 5: Separation of meltpool body and ejecta using image processing: (a) original image, where the meltpool body is indicated by a square of 40 ×40 pixels; (b) and (c) separated meltpool and ejecta images, respectively, used for extracting temperature-based features; (d) and (e) are binarized meltpool and ejecta images used for extracting shape-based features. Red arrows refer to the Euclidean distance measured from the center of the meltpool body.

(a) Meltpool Length (L_m)

The Meltpool Length (L_m) is defined as twice as the largest distance from the center of the meltpool to its edge as visually depicted in Figure 5(d). It was calculated from each frame of the meltpool image obtained from the pyrometer as follows

$$L_m = 2d_{max}, \tag{3}$$

where d_{max} is the largest Euclidean distance from the center of meltpool to its edge.

The meltpool length was related to part quality in the literature. For example, Guo et al. (2019) relate the meltpool shape and size to the build quality. Among different experimental studies conducted by Guo et al. (2019), meltpool length was observed to increase as a function of laser power and scanning speed, even when the energy density was held constant. Heigel and Lane (2018) observed a similar increasing trend with the laser power.

Recently, Li et al. (2021) also confirmed the increase in meltpool length as a function of both laser power and scanning speed, using theoretical simulation of meltpool which resulted in meltpool images similar to those observed in this work (Figure 4, Sec. 2.4). In other words, increasing laser power within the extent of conduction mode regime, typically results in an overall increase in the meltpool size, while increasing the scanning speed results in meltpool elongation, i.e., increase in meltpool length and decrease in width. We note that the meltpool shape is also contingent on other factors such as the scanning strategy (Oliveira et al., 2020a).

The elongation of the meltpool as a function of scanning velocity was similarly observed in theoretical meltpool-scale simulations by Khairallah et al. (2016). They concluded that the elongation of the meltpool at high scanning speeds (relative to the laser power) is symptomatic of a phenomenon called balling. To explain further, the elongated meltpool breaks into separate chunks (balling) on account of the Plateau-Rayleigh effect at higher scanning speeds. These discrete meltpool parts fail to completely coalesce on solidification, resulting in incomplete fusion, and subsequent formation of porosity. The onset of balling was recently observed by Gaikwad et al. (2020) in the sintering of single track LPBF parts who reported that a P/V ratio of less than 0.5 [J·mm^{-1}] resulted in balling. Thus, the meltpool length is considered an important indicator of the process regime in LPBF.

(b) Mean Ejecta Spread (S_e)

The Mean Ejecta Spread (S_e) feature is intended to capture the distance travelled by the ejecta particles and represents the spatial distribution (spread) of spatter particles. It was quantified as the average distance measured from the center of the meltpool to every ejecta pixel as indicated by arrows in Figure 5(e). We note that the ejecta is demarcated as the rest of the meltpool other than the body (1160 μm ×1160 μm). The mean ejecta spread is estimated as follows

$$S_e = \frac{1}{n}\sum_{i=1}^{n} d_i^e \,, \tag{4}$$

where n is the total number of nonzero ejecta pixels and d_i^e is the Euclidian distance from meltpool center to the i^{th} ejecta pixel. For example, examining S1 – S5 in bottom row of Figure 4, the ejecta spread decreases with decrease in scanning speed. Thus, S_e captures the average distance travelled by each ejecta particle. In this work, based on the following key findings concerning the ejecta distribution, quantity, and induced flaw formation from the literature, spread of ejecta (S_e) was chosen as one of the main predictors of porosity.

Nassar et al. (2019) attributed formation of large ejecta to two effects based on high-speed imaging: (i) inelastic collision between powder particles that are removed from the laser-powder interaction zone, and (ii) the coalescence of partially fused particles. These ejecta particles were found to disturb the meltpool stability and result in lack-of-fusion porosity. Ali et al. (2019) showed that the ejecta tends to become more violent and extend farther from the meltpool due to the onset of meltpool instability. The authors correlated the phenomenon of ejecta spread to the increased porosity.

In a similar study, Esmaeilizadeh et al. (2019) investigated the effect of ejected spatter particles on the quality of the parts produced by LPBF. The authors compared the parts printed on ejecta rich regions with those printed on virgin powders and observed that the ejecta rich regions of the build plate resulted in parts with higher porosity. Ly et al. (2017) studied the underlying phenomena of ejecta formation in LPBF, both experimentally and through simulation. The authors observed that the angle of ejection is significantly dependent on processing parameters, namely, laser power and scanning speed.

The spread of ejecta has also been linked with the direction of argon gas flow in LPBF. For example, Schwerz et al. (2021) observed that ejecta particles travel farther in the direction of gas flow and result in porosity in regions of the part away from the gas inlet. Qiu et al. (2015) studied the interaction between laser beam and powder particles both experimentally and through modeling approaches. Apart from reporting that increased scanning speed (V > 2700 mm·s^{-1}) and powder layer thickness ($T > 40\mu m$) lead to porosity formation in LPBF, they further concluded that the porosity is linked to the meltpool instability and ejecta spread.

In a similar vein, Repossini et al. (2017) used the characteristics of ejecta formation such as statistical features in a logistic regression model to predict flaw formation in LPBF. The authors underscored the effectiveness of ejecta characteristics in determining the build quality, represented by under-melted, normal-melted, or over-melted parts. Hence, based on these prior results, linking the spread (spatial distribution) of ejecta to porosity we derived the S_e metric.

(c) Mean Ejecta Temperature (T_e)

The Mean Ejecta Temperature (T_e) is the average temperature of the ejecta (Figure 5(b)), and it was calculated as follows

$$T_e = \frac{1}{n}\sum_{i=1}^{n} T_i \,, \tag{5}$$

where n is the total number of nonzero ejecta pixels and T_i is the temperature of i^{th} pixel.

In the literature, the temperature of the ejecta is closely associated with the onset of meltpool instability, which is also contingent on the material type and is influenced by the partial vapor pressures of the elements that compose the material (Khairallah et al., 2016). For example, during the LPBF processing of 17-4 PH stainless steel, Ali et al. (2019) noticed that unstable meltpool tends to eject hot spatter particles. Ly et al. (2017), demarcated two types of particles (depending on temperature) that are ejected from the meltpool in the LPBF process. These were broadly termed hot and cold particles (ejecta). The difference between the two types of particles ejected is that the hot particles result from interaction of the particle with the laser beam. Hot particles typically reach the melting point of the material and are in a completely or partially molten state.

Fedina et al. (2021) hypothesized that high temperature ejecta that results from hot particles can interact with the virgin powder particles after landing on the bed, leads to agglomeration of fused particles. In contrast, cold particles, as explained by Ly et al. (2017), are powder particles that discharge from the laser-powder interaction zone, but do not interact with the laser beam. The collision between ejecta particles may result in a merger and consolidation into a larger particle after cooling. These larger particles settling on the powder bed can lead to lack-of-fusion defects in the subsequent layers in LPBF parts (Darvish et al., 2016). Since these agglomerates are usually larger than the feedstock material and therefore, become a source of powder contamination, which also promotes formation of lack-of-fusion porosity.

(d) Distribution of Meltpool Temperature (Sk_m)

The temperature distribution of the meltpool region shown in Figure 5(b) is quantified in terms of its skewness (third moment of the mean) as follows

$$Sk_m = \frac{\frac{1}{m}\sum_{i=1}^{m}(T_i - \mu)^3}{\sigma^3}, \tag{6}$$

where μ is the mean of meltpool temperature, σ is the standard deviation of meltpool temperature and m is the total number of nonzero pixels in the meltpool temperature image.

The skewness feature captures the symmetry of the meltpool temperature distribution about the mean. Results from the literature indicate that the temperature distribution of the meltpool is symptomatic of meltpool instability and consequently relates to flaw formation.

Romano et al. (2015) suggested that the temperature distribution of the meltpool in LPBF plays a critical role in determining the final part quality, including porosity level in the part. The geometry of the liquidous region of meltpool and the amount of liquid material, which is at a temperature greater than the melting point of the material being processed, is dependent on the processing conditions. Ly et al. (2017) simulated meltpool behavior in LPBF and observed that processing at a relatively low scanning speed resulted in a deep meltpool depression with a large amount of liquid material. Increasing laser power and scanning speed changed the meltpool shape and temperature significantly, resulting in a shallower and elongated meltpool.

2.6 Machine Learning for Porosity Prediction

The meltpool features described in Sec. 2.5 were used as inputs to supervised machine learning models trained towards the following two tasks. Task 1 – detection of type of porosity or process regime (lack-of-fusion, conduction, keyhole formation); and Task 2 – classification of the severity of porosity. These machine learning-based classification tasks are summarized in Table 3 and Figure 6.

The type of porosity was classified into three modes: lack-of-fusion, conduction mode (ideal case, minimal porosity), and keyhole formation based on optical and scanning electron microscopy. Depending on the volume of the porosity detected in the part in term of defect volume ratio (DVR from XCT) and Archimedes relative density (ρ_{rel}), the severity of porosity was discretized into different levels. The discretization ranges from a 2-way (high and low) classification to higher resolution 5-way classification. The basis for this demarcation is explained in detail in Sec. 3.2.

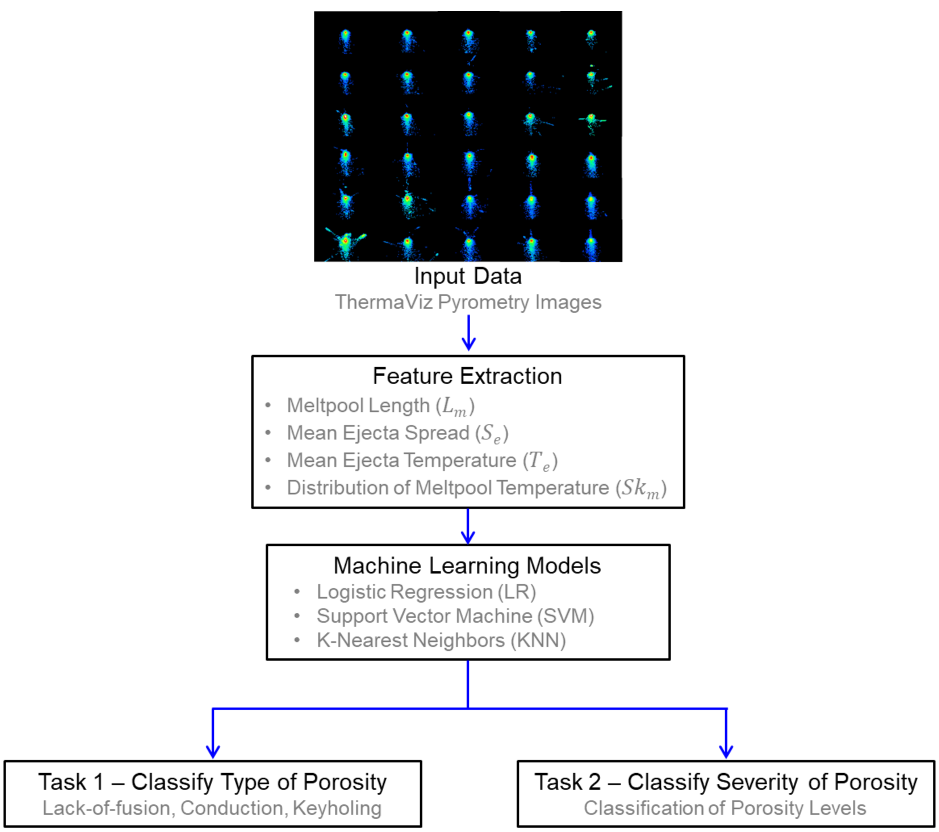

Figure 6: Schematic representation of data processing and machine learning approach used in this work for classifying severity and type of porosity.

Table 3: The various machine learning tasks implemented in this work. The aim is to classify the type and severity of porosity at various levels.

Task 1 – Classify Type of Porosity (Process Regime)		
Classification Level	Porosity Mode	Number of Meltpool Images Per Class
3-way	1. Lack-of-fusion porosity 2. Conduction mode (ideal case, minimal porosity) 3. Keyhole formation	3,500
Task 2 – Classify Severity of Porosity		
Classification Level	Severity of Porosity	Number of Meltpool Images Per Class
2-way	1. Nominal (DVR= 0.00%, and $\rho_{rel} \geq$ 99%) 2. Porous (DVR> 0.00%, and $\rho_{rel} \geq$ 86%)	10,000
3-way	1. Nominal (DVR= 0.00%, and $\rho_{rel} \geq$ 99%) 2. Medium (0.08% < $DVR \leq$ 0.61%, and $\rho_{rel} \geq$ 93%) 3. High (DVR> 1.00%, and $\rho_{rel} \leq$ 90%)	5,600
4-way	1. Nominal (DVR= 0.00%, and $\rho_{rel} \geq$ 99%) 2. Low (0.00% < $DVR \leq$ 0.08%, and $\rho_{rel} \geq$ 97%) 3. Medium (0.08% < $DVR \leq$ 0.61%, and $\rho_{rel} \geq$ 93%) 4. High (DVR > 1.00%, and $\rho_{rel} \leq$ 90%)	5,600
5-way	1. Nominal (DVR= 0.00%, and $\rho_{rel} \geq$ 99%) 2. Low (0.00% < $DVR \leq$ 0.08%, and $\rho_{rel} \geq$ 97%), 3. Medium (0.08% < $DVR \leq$ 0.61%, and $\rho_{rel} \geq$ 93%) 4. High (0.61% < $DVR \leq$ 1.38%, and $\rho_{rel} \geq$ 90%) 5. Very High (1.38 < $DVR \leq$ 1.96%, and $\rho_{rel} \geq$ 86%)	3,000

The machine learning classification models used in this work are basic supervised machine learning models, namely, K-Nearest Neighbors (KNN), Support Vector Machine (SVM), and logistic regression (LR). These models were chosen given their ease of implementation and computationally tractable nature. For example, KNN is considered one of the simplest and readily implemented machine learning classification models, with no complex activation function and computation of chain derivatives as with neural networks (Mucherino et al., 2009). It can in turn be potentially implemented with rudimentary computational processing on board a LPBF machine with sparse computational resources.

The classification results obtained from KNN, SVM, and LR are compared with a complex deep-learning convolutional neural network (CNN). The CNN does not use the physics-informed features, but instead learns to discern the type and severity of porosity directly from raw meltpool images – an inherently data and computationally intensive process. A detailed explanation of the implementation of the CNN is provided in Appendix A.

The training and testing process of the machine learning models is explained for the 4-way pore severity classification. The approach remained same for all machine learning tasks. For the 4-way pore severity classification study a total of 22,400 data points (meltpool images) were available (5600 data points per class). Out of these, 17,920 data points (80%) were used to train and validate the models and the remaining 4480 data points are used for testing. For hyperparameter optimization, a 5-fold cross-validation and sequential Bayesian optimization schema was used. The accuracy of prediction for the various machine learning models was quantified in terms of the F1-score, which ranges between 0 and 1 (highest accuracy); false positive rate (FPR, Type I error rate); and false negative rate (FNR, Type II error rate) (Wardhani et al., 2019).

3 Results

3.1 Porosity Characterization Using SEM and Optical Microscopy

Figure 7 (top two rows) shows the SEM images obtained in the X-Z directions of the segments (P1 – P5, S1 – S5) built under varying process conditions. In Figure 7 two SEM images were captured at different scales are shown for each processing condition. In context of P1 – P5, pores were not observed until the laser power is reduced to 120 W (P5), at which juncture a lack-of-fusion type of pore is noted. Such lack-of-fusion porosity is characterized by its irregular shape, and it caused due to insufficient energy to melt the powder (Snow et al., 2021).

As evident in Figure 7 (bottom two rows), the lack-of-fusion porosity increases proportionally to the scanning speed due to decrease in the energy density (E_v). In the scanning speed range of 2200 mm·s^{-1} (S3) to 3780 mm·s^{-1} (S1) (E_v, 23 to 40 J·mm^{-3}) lack-of-fusion porosity is prominent. Apart from their characteristic irregular shape, partially melted powder particles are observed in the voids in the bottom two rows of Figure 7.

On decreasing the scanning speed to V = 1320 mm·s^{-1} with P = 370 W, which corresponds to an increased energy density (E_v = 67 J·mm^{-3}), lack-of-fusion porosity was largely eliminated. However, with a further reduction in scanning speed to V = 880 mm·sec^{-1}, resulting in E_v = 100 J·mm^{-3} in segment S5 (the highest level of E_v in this work), keyhole type porosity was observed. Keyhole porosity forms at high energy density levels as the laser penetrates deeper into the deposited material, causing material to vaporize (King et al., 2014). The resulting cavity in the part collapses, causing a pore typically in the range of 30 – 50 µm. Thus, the scanning speed experiments manifest in transition of porosity from lack-of-fusion to keyhole porosity. While such high energy density values can cause both keyhole porosity and gas porosity (Snow et al., 2020), however, under high-resolution scanning electron microscopy, the pores in region S5 (Figure 7) were observed to have an irregular shape characteristic of keyhole formation, as opposed to the uniform circular shape typical of gas porosity.

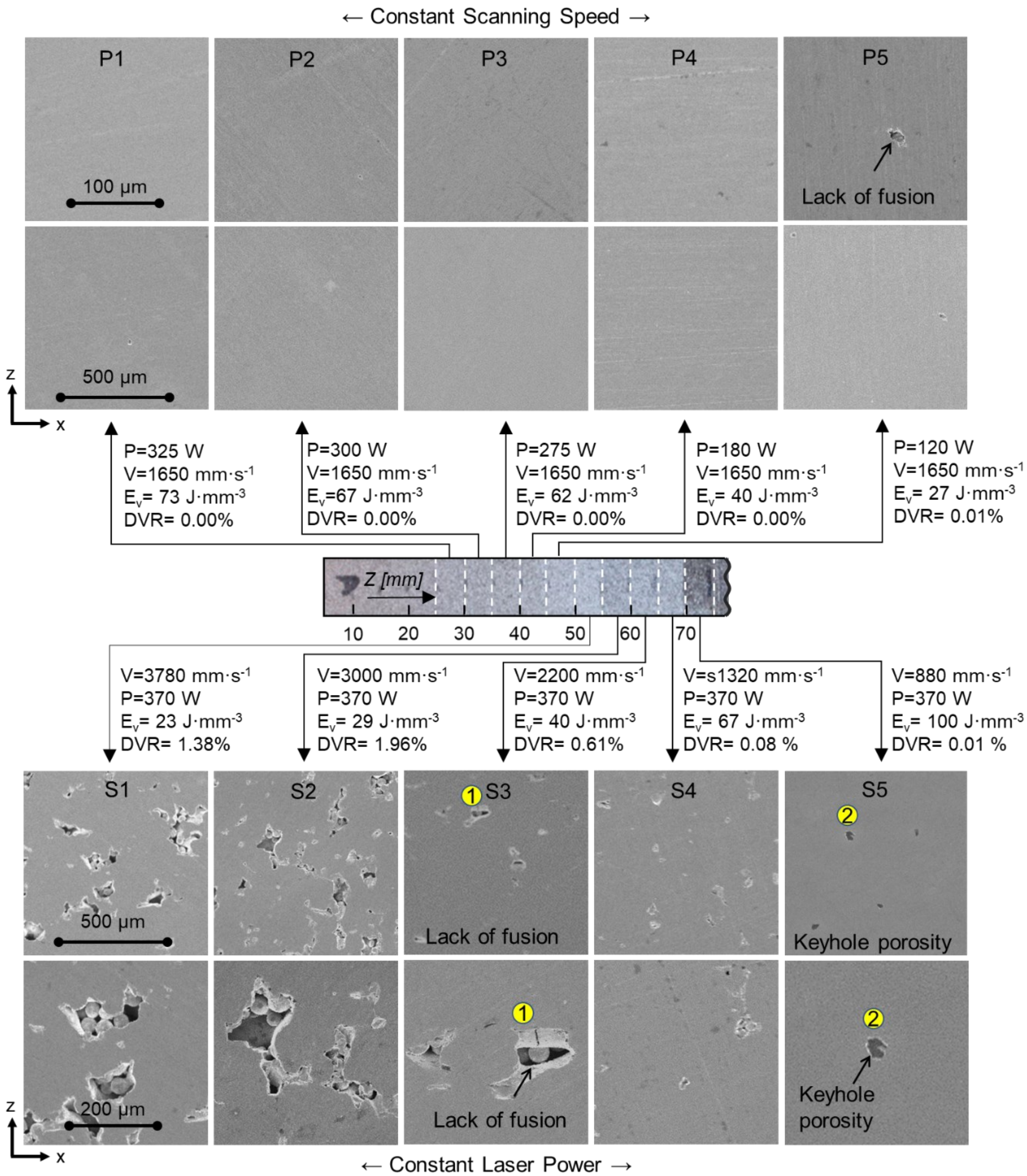

Figure 7: (Top Row) SEM images of the XZ- cross sections of the segments processed under varying laser power while the other processing parameters maintained constant (V =1650 mm·s^{-1}, H = 0.090 mm, and T = 0.030 mm). The porosity content corresponding to different laser powers remains insignificant while in the laser power range of 325 W to 180 W (P1 - P4). Lack-of-fusion pores are observed in the segment P5 processed at a lower laser power (120 W). (Bottom Row) SEM images of the XZ-cross sections of the segments processed under varying scanning speed while the other processing parameters maintained constant (P =300 W, H = 0.140 mm, and T = 0.030 mm). Segments S1 – S3 processed under very high scanning speed (3000 – 3780 mm·s^{-1}) are replete with large lack-of-fusion pores. The porosity is mitigated as the scanning speed is reduced. Keyhole pores are observed in the S5 segment processed at the lowest scanning speed (880 mm·s^{-1}).

The severe lack-of-fusion porosity observed at the highest scanning speed range of 2200 mm·s^{-1} (S3) to 3780 mm·s^{-1} (S1) in this experiment is explained by a phenomena called balling, which is a result of meltpool instability due to the Plateau-Rayleigh effect (Khairallah et al., 2016). Considering a deposition track as cylinder of liquid metal with diameter D and length L, Scipioni Bertoli et al. (2017) suggested that the condition for Plateau Rayleigh meltpool instability is satisfied when L/D > π. Under this condition, the meltpool track breaks down into small droplets to minimize its surface energy. King et al. (2015) observed a similar phenomenon during the meltpool simulation in LPBF process in meltpool-level theoretical simulations. They noted balling of the meltpool at a relatively high scanning speed while processing the first layer on the top of virgin powder. In the simulation studies of King et al. (2015), balling was mitigated as the scanning speed was decreased. Guo et al. (2020) observed a similar type of balling-initiated porosity as the scanning speed was increased to 3000 mm·s^{-1} (E_v= 29.63 J·mm^{-3}) during the LPBF processing of Inconel 738LC.

To explain these observations further, Figure 8 compares the optical micrographs of individual samples from three modes of processing conditions as observed from XY- and XZ- planes: severe lack-of-fusion, represented by high-speed processing condition S2 (P =370 W, V = 3000 mm·s^{-1}, Figure 8(a) and (b)) ; conduction mode, represented by nominal processing condition P0 (P =370 W, V = 1650 mm·s^{-1}, Figure 8(c) and (d)); and keyholing mode, represented by low scanning speed processing condition S5 (P =370 W, V = 880 mm·s^{-1}, Figure 8(e) and (f)). We note that during the processing of segment S5, referring to Figure 8(f), the pores are observed to form near the bottom of the meltpool track, and have an irregular funnel-like shape characteristic of keyhole formation.

While continuous meltpool tracks are observed for both the nominal (Figure 8(c) and Figure 8 (d)) and keyholing regime (Figure 8(e) and Figure 8(f)), partial fusion of tracks is noticed for the lack-of-fusion mode (Figure 8(a) and (b)). In the literature, Guo et al. (2020) related the scanning speed to the viscosity of melt track during solidification and suggested that the reduced energy density at high scanning speed results in a viscous meltpool that does not flow sufficiently to wet the adjacent tracks.

Subsequently, the powder in a layer is not uniformly melted resulting in lack-of-fusion porosity. Similarly, Qiu et al. (2015) attributed severe lack-of-fusion porosity to meltpool instability, which increases with scanning speed and results in discontinuous tracks and violent ejecta.

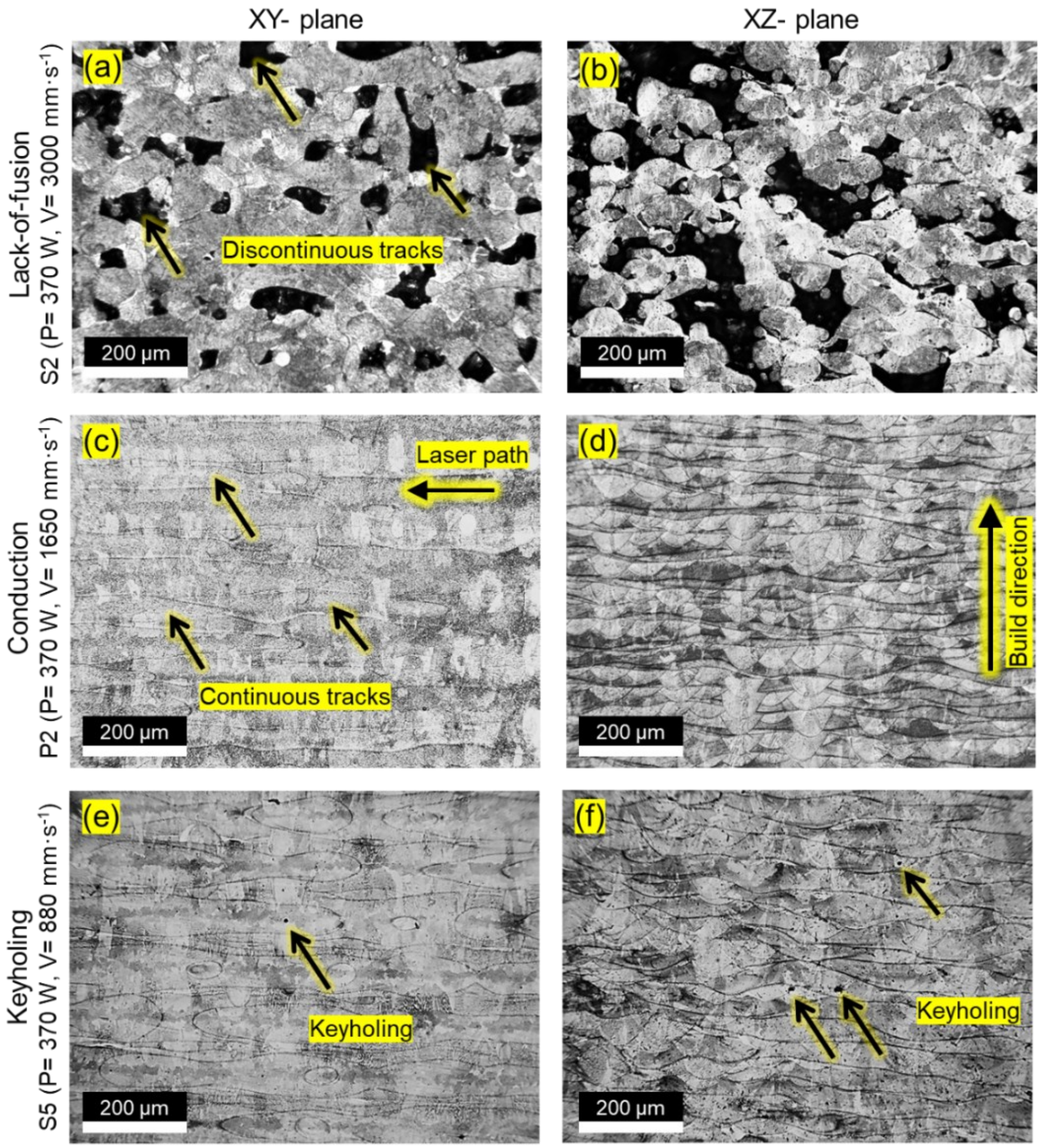

Figure 8: Optical microscopy images of the LPBF-processed ATI 718Plus alloy: (a) and (b) are optical images in the XY- and XZ- planes, respectively, of segment S2 (P = 370 W, V = 3000 mm·s^{-1}). This condition represents severe lock-of-fusion porosity due to balling effect. (c) and (d) are the optical images of segment P2 (P = 300 W, V = 1650 mm·s^{-1}) in the XY- and XZ- planes, respectively. This condition is a representative of the ideal conduction mode, where continuous tracks are observed along the laser path with no porosity detected. Finally, (e)and (f) are the optical images of segment S5 in the XY- and XZ- planes, respectively, in which keyhole porosity is observed.

3.2 Pore Severity Quantification using XCT and Archimedes Method

The severity of porosity observed in the test part from the XCT is summarized in Figure 9. The porosity level in term of the defect volume ratio (DVR) for this work ranges from 0% to 2%. The highest variation in DVR is observed in the segments (S1 – S5), where the laser scanning speed was varied. In this work, the effect of laser power on porosity density (P1 – P5) was found to be insignificant in comparison with scanning speed, except for the segment P5, where the laser power is greatly reduced to 120 W as shown in the inset of Figure 9. In segment P5 the porosity is observed to be 0.01%. Summarized in Figure 9 are also the relative density measurements from the Archimedes method (ρ_{rel}), which ranges from ~99% to 86.5%.

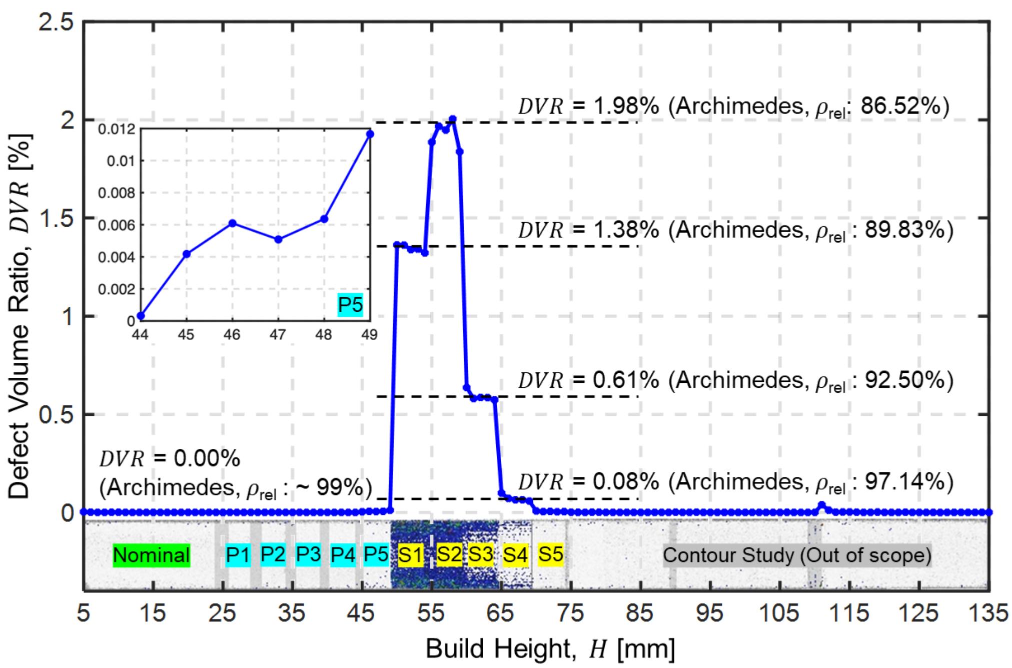

Figure 9: XCT analysis of the part showing the effect different processing parameters on the overall defect volume ratio (DVR) and relative density (ρ_{rel}). Four clusters of part porosity are evident.

The DVR and relative density (ρ_{rel}, Archimedes) are reported in Table 4. Based on these, the severity of porosity can be divided into multiple discrete categories. For example, in Figure 9 the porosity can be demarcated into four classes, as Nominal (DVR= 0.00%, ρ_{rel} ≥ 99%), Low (0.00% < DVR ≤ 0.08%, ρ_{rel} ≥ 97%), Medium (0.08% < DVR ≤ 0.61%, ρ_{rel} ≥ 93%), and High (DVR > 1.00%, ρ_{rel}: ≤ 90%). To further elucidate these observations, the effect of volumetric energy density on severity of porosity is discussed herewith. We note that for ease of explanation, we will mainly focus our analysis on the 4-way classification of pore severity demarcated above.

Practitioners often use E_v as an approximate guide to set LPBF process parameters for a material class with the aim of mitigating porosity (Kasperovich et al., 2016). However, E_v is affected by other factors beyond the main process parameters, such as laser spot size, scan strategy, gas flow, material properties, and the size of powder particles, which limit its transferability between different materials, processing conditions, and machines (Oliveira et al., 2020b). To mitigate porosity formation, E_v should be sufficiently large (contingent on the type of material) to achieve complete melting and fusion of the powder particles (Gibson et al., 2021). When the E_v is inordinately low, lack-of-fusion porosity is observed as explained in the context of Figure 7. Likewise, very high E_v should be avoided to prevent vaporization of the material and entrapment of gases, which lead to gas (pinhole) porosity and keyhole porosity, respectively (Gibson et al., 2021). However, it should be noted that porosity formation in LPBF process is a function of several factors beyond process parameters. Material characteristics, build condition, part shape, location of the part on the build plate, among others, are linked to porosity formation. Hence, E_v alone is an insufficient quantifier of porosity (Giovagnoli et al., 2021).

The effect of E_v on porosity is shown in Figure 10 in terms of XCT volumetric analysis. The top row of Figure 10 corresponds to segments P1-P5 where the laser power (P) was decreased from 325 W to 120 W, while keeping the scanning speed (V) constant at 1650 mm·s^{-1}. Consequently, E_v decreases proportionally from 73 J·mm^{-3} at 325 W to 27 J·mm^{-3} at 120 W. No significant porosity is observed in the build (DVR = 0.00%) when using a laser power between P = 325 W (73 J·mm^{-3}) to 180 W (40 J·mm^{-3}). However, pores appear with decrease in laser power to P =120 W, which corresponds to an E_v=26 J·mm^{-3}, resulting in a DVR = 0.01%.

Table 4 Archimedes measurements corresponding to the defect volume ratio (DVR) for each processing condition (section) of the part.

Process Step		Laser Power P [W]	Scanning Speed V [mm×s^{-1}]	Hatch Spacing H [mm]	Archimedes Relative Density, ρ_{rel} [%]	XCT Defect Volume Ratio, DVR [%]
Nominal		300	1650	0.09	99.285	0
Variation in Laser Power	P1	325			99.054	0
	P2	300			98.796	0
	P3	275			99.733	0
	P4	180			99.947	0
	P5	120			98.564	0.01
Variation in Scanning Speed	S1	370	3780	0.14	89.833	1.38
	S2		3000		86.522	1.96
	S3		2200		92.504	0.61
	S4		1320		97.142	0.08
	S5		880		98.997	0.01

In a similar vein, from the bottom row of Figure 10 it is observed that an increase in the scanning speed, which reduces E_v, leads to an increase in the porosity level. For example, the scanning speed setting of V = 3000 mm·s^{-1} with P = 370 (S2), corresponding to E_v = 29 J·mm^{-3} results in a DVR of nearly 1.96%. An insight from Figure 10 is that the porosity level in the build is generally mitigated by reducing the scanning speed and consequently increasing the energy density. Another observation from Figure 10 is that the majority of the pores are concentrated within a distance of 3 mm near the edges. This is because, the central area of an LPBF part is generally at an elevated temperature compared to the edges (Pantawane et al., 2020), which facilities fusion of powder particles and thereby mitigates the lack-of-fusion porosity. Recently, concentration of porosity near the edge has also been observed by Diehl and Nassar (2020).

However, using the energy density as a sole measure to control porosity may result in contradictory results. For instance, referring to Figure 8, the same energy density of E_v= 40 J·mm^{-3} is obtained for condition P4 (P = 180 W and V = 1650 mm·s^{-1}) and condition S3 (P = 370 W and V = 2200 mm·s^{-1}). However, in P4 the DVR = 0%, while in the latter DVR ~ 0.6%. Another anomalous behavior observed in Figure 10 is that the segment S2 processed at the highest scanning speed (V= 3780 mm·s^{-1}) with E_v= 23

J·mm^{-3} has a DVR = 1.38%. However, this level of porosity is lower for S2 which is processed at V = 3000 mm·s^{-1} (E_v= 29 J··mm^{-3}) and has a DVR= 1.96%.

This outcome in the context of Figure 10 indicates that the energy density is not a viable universal parameter that can be reliably used to correlate with the porosity severity in LPBF as indicated in the recent literature (Oliveira et al., 2020b). Similar shortcoming with E_v has been noted by previous researchers. For example, Tang et al. (2017) found that utilizing the same energy density (E_v) obtained by changing different process parameters in LPBF resulted in different levels of lack-of-fusion porosity in the part. Similar results cautioning the reliability of E_v were reported by Giovagnoli et al. (2021), who studied the limitation of volumetric energy density as an approach to estimate the severity of porosity in LPBF.

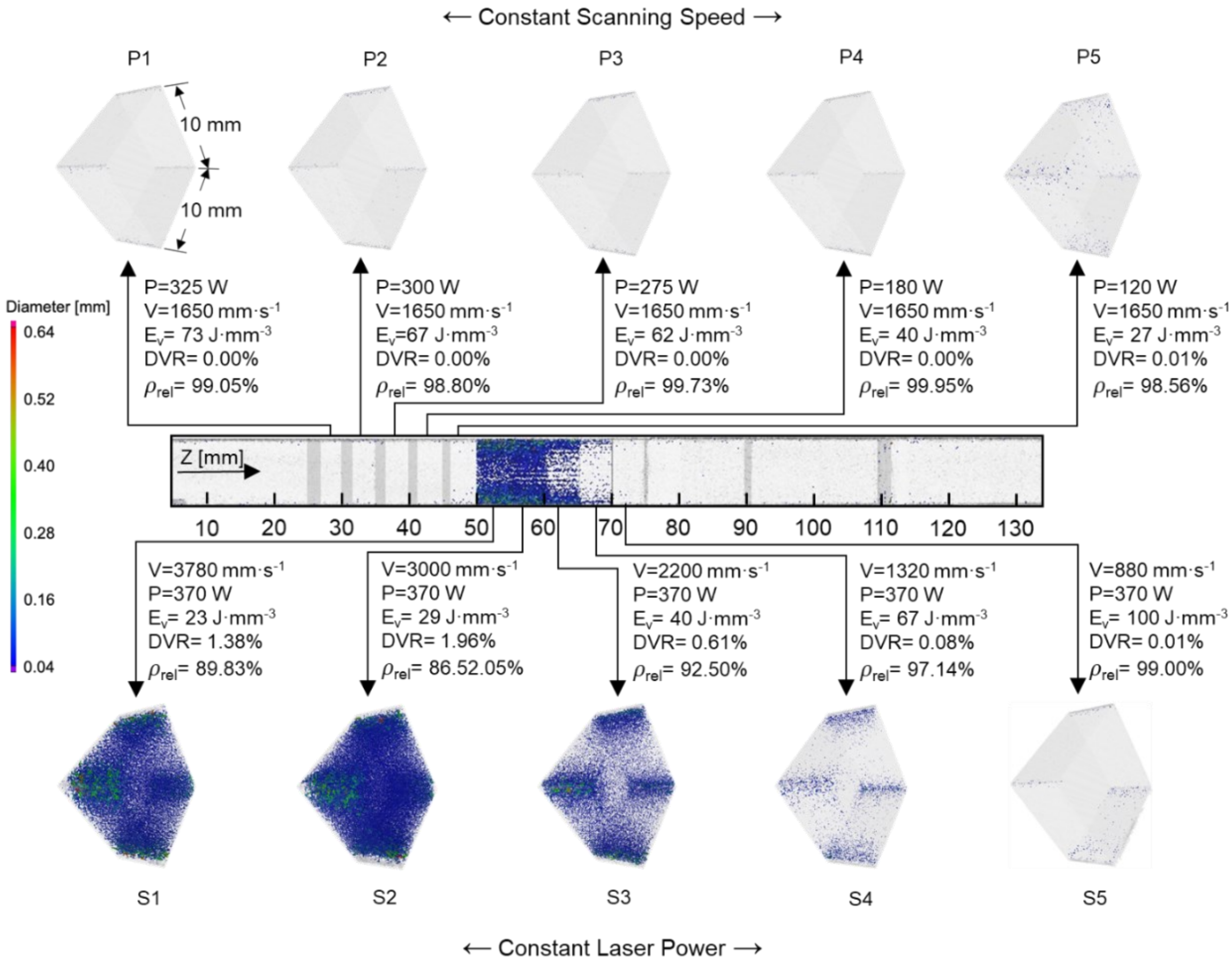

Figure 10: XCT analysis of the various sections showing the effect of laser power (P) and scanning speed (V) on porosity in 3D. DVR is the defect volume ratio from Volume Graphics software while ρ_{rel} is the relative density measured using Archimedes method.

One of the main shortcomings with the volume energy density (E_v) that hampers its generalizability is that it does not include the material properties. To overcome this gap, recently, Rankouhi et al. (2021) proposed a dimensionless number that aggregates LPBF process parameters and thermophysical properties of the material. Further, this dimensionless number was related to relative density of a variety of metal alloys. The dimensionless number (Π_1) is expressed as,

$$\Pi_1 = \frac{C_p\, P}{k\, V^2\, h} \tag{7}$$

where C_p is specific heat [J·kg^{-1}·K^{-1}], P laser power [W], k thermal conductivity [W·K^{-1}·m^{-1}], V laser scanning speed [m·s^{-1}], and h hatch spacing [m].

Based on analysis of data from literature, Rankouhi et al. (2021) observed that for a fully dense as-built part, the dimensionless number should be in the range of $61 < \Pi_1 < 146$, which defines an optimal window for selecting process parameters that results in maximum density. Parts built outside this range consistently have a lower density. For $\Pi_1 < 61$, the density is reduced due to lack of fusion porosity while for $\Pi_1 > 146$ it is reduced due to keyhole or gas porosity. Rankouhi et al. (2021) proposed a relationship between the relative density of as-built part and the dimensionless number (Π_1) determined by statistical analysis of results reported in the literature. The relative density of a part (ρ_{rel}) as a function of Π_1 is,

$$\rho_{rel} = e^{-2.391\times10^{-5}\times\Pi_1} - 0.15e^{-0.06688\times\Pi_1} \tag{8}$$

We used the above relationship to verify the experimental observations reported in Sec. 3.2 (Figure 9 and Table 4). For this purpose, we used the Archimedes method to measure the density of test coupons (ρ_{rel}). Figure 11 correlates the dimensionless number (Π_1) with both the measured density from Archimedes method and predicted relative density (ρ_{rel}) from Eq. (8). It is observed that the measured density closely follows the predicted density with equivalent labeling of the porosity type demarcated by Rankouhi et al. (2021).

Based on the dimensionless number (Π_1), as shown in Figure 11, most of the porosity observed in this work falls in the lack-of-fusion region. The onset of lack-of-fusion porosity was observed for $\Pi_1 < 41$, while keyhole melting was observed for $\Pi_1 > 126$. These match closely with the observations of Rankouhi *et al.* (2021) who suggest the onset of lack-of-fusion at $\Pi_1 < 61$ and keyhole at $\Pi_1 > 146$.

The slight discrepancy between the observed relative density values and those predicted by Rankouhi *et al.* (2021) from Eqn. (8) is attributed to the novelty of the material studied in this work (ATI 718Plus). This material is not present in the data set examined by Rankouhi *et al.* (2021). Moreover, Eqn. (8) was derived through statistical regression analysis of porosity observed in eight different LPBF materials ranging from low melting temperature alloys, such as Copper and AlSiMg10 to extreme temperature Nickel-based superalloys and Tungsten. This materials-related distinction also explains the difference in the Π_1 regime demarcations between our work and Rankouhi *et al.* (2021).

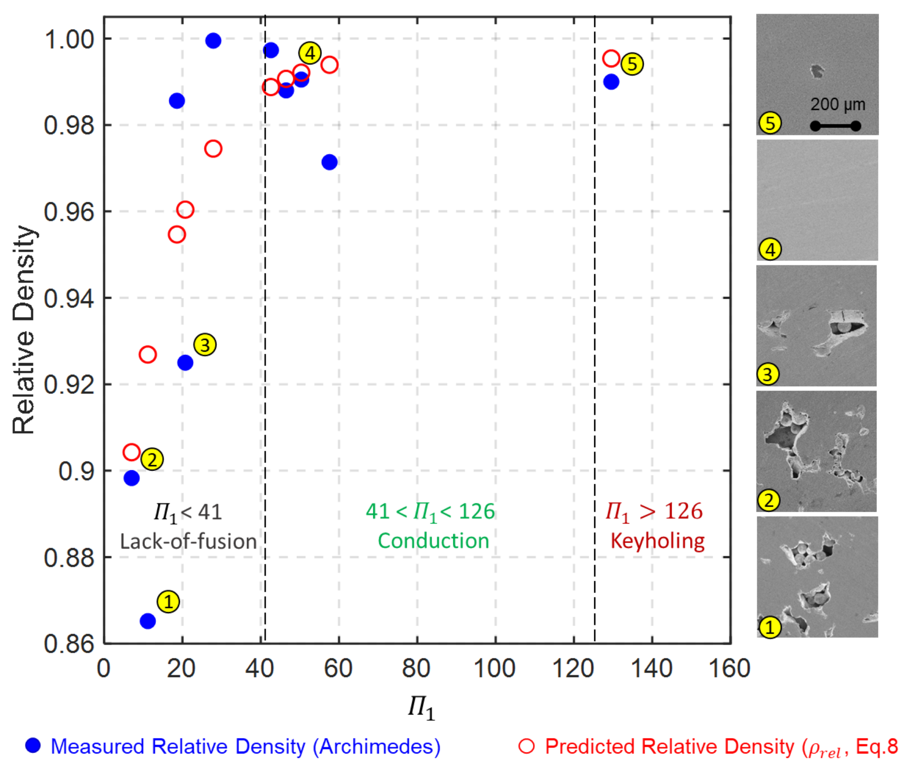

Figure 11: Porosity classification based on relative density as a function of dimensionless number Π_1. SEM images on the right represent the actual porosity type corresponding to points numbered inside the figure. Lack-of-fusionn porosity is observed for $\Pi_1 < 41$, conduction regime (minimal prorosity) for $41 < \Pi_1 < 126$, and Keyhole formation for $\Pi_1 > 126$.

3.3 Prediction of Porosity Using Meltpool Signatures and Machine Learning

The aim of this section is to predict the severity of porosity as a function of the meltpool signatures extracted from the pyrometer (described in Sec.2.5). For illustration, the XCT for the four levels of porosity levels observed at different processing conditions are depicted in Figure 12 and visually correlated with the meltpool signatures.

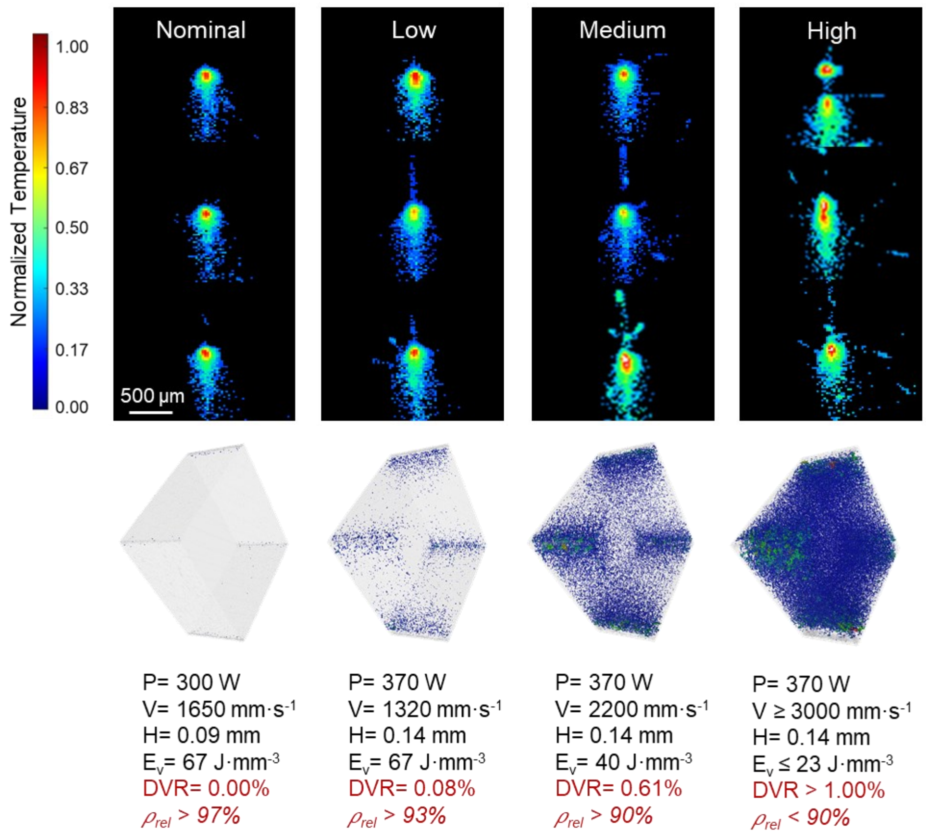

Figure 12: Correlation of porosity levels with meltpool images acquired from the dual wavelength imaging pyrometer. The shape, size, and temperature of meltpool and ejecta change with porosity level in the part.

Figure 13 shows the correlation between different features extracted from the dual-wavelength imaging pyrometer frames, and the level of porosity. As depicted in Figure 13, the relationships between the two shape-based features (Meltpool Length (L_m) and Mean Ejecta Spread (S_e)) and the two temperature-based features (Skewness of Meltpool Temperature (Sk_m) and Mean Ejecta Temperature (T_e)), have complex trends.

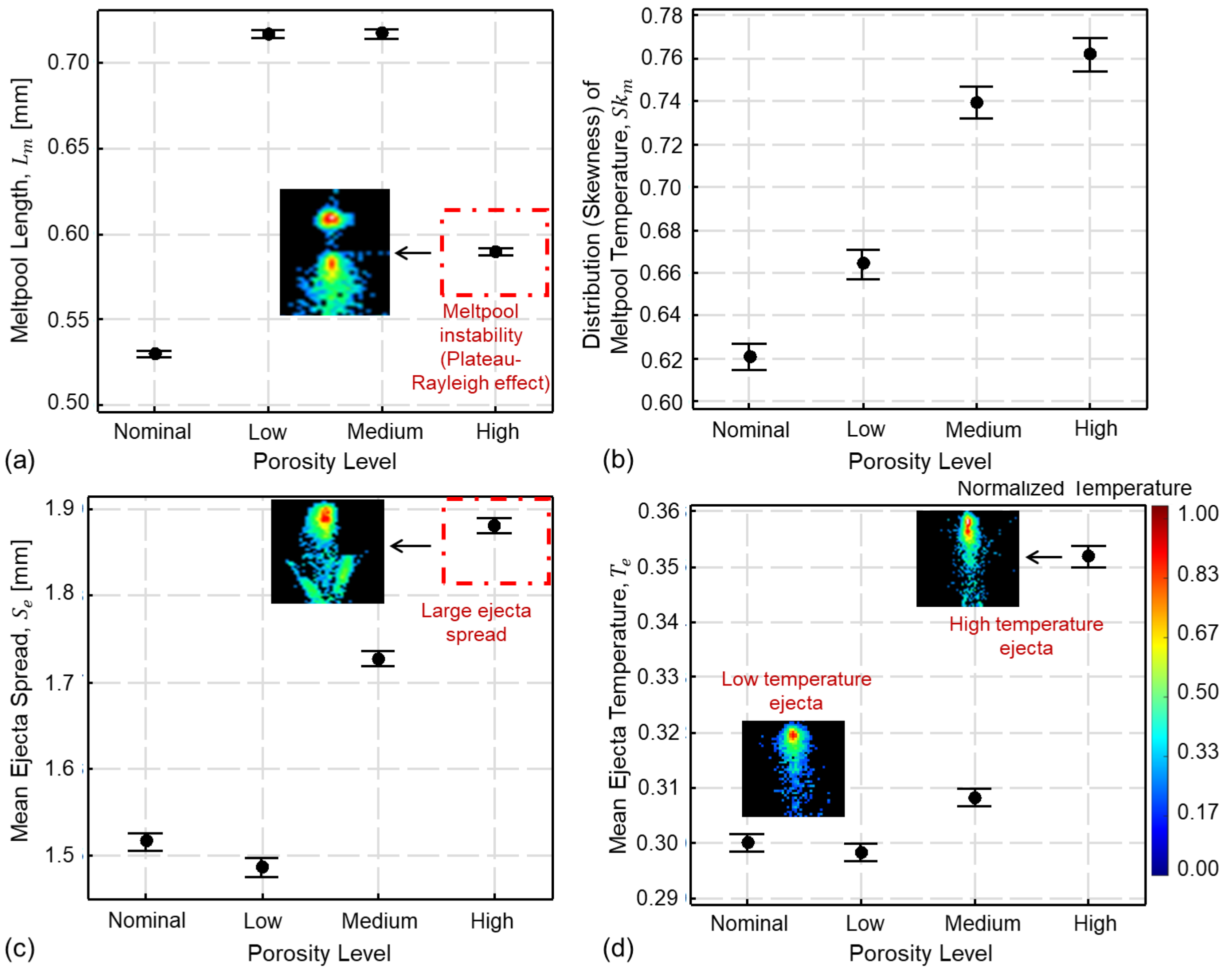

Figure 13: Shape and temperature-based statistical features extracted from pyrometry images, including (a) Meltpool Length (L_m), (b) Distribution of Meltpool Temperature (Sk_m), (c) Mean Ejecta Spread (S_e), and (d) Mean Ejecta Temperature (T_e), as a function of the four porosity levels depicted in Figure 9.

For example, as shown in Figure 13(a), the meltpool length is smaller for the Nominal porosity (DVR= 0.00%, $\rho_{rel} \geq 99\%$) condition. The meltpool elongates as the processing condition deviates from the nominal, and ultimately breaks down for processing condition (S2) where High porosity level ($DVR >$ 0.61%, $\rho_{rel} \leq 90\%$) was observed. The breakdown of the meltpool at higher scanning speeds was explained before in Sec. 3.2 as a consequence of the Plateau-Rayleigh effect (Guo et al., 2019). The breakdown of the meltpool into separate chunks of molten material leads to poor fusion as depicted in Figure 8(a).

The meltpool and ejecta temperature are correlated with porosity levels in Figure 13(b) and (d), respectively. It is observed that both the skewness of meltpool temperature (Sk_m) and the mean ejecta temperature (T_e) show an increasing trend with porosity level. To explain further, the meltpool temperature distribution (Sk_m) captures the symmetry of the meltpool temperature distribution. High Sk_m indicates increase in skewness and asymmetry. As shown in Figure 13(b), Sk_m increases linearly with the porosity level in the part. The increasing positive skewness indicates that a large area of the meltpool has low temperature values. Hence, there is insufficient thermal energy to completely fuse powder particles together, resulting in lack-of-fusion porosity.

The spread of ejecta (S_e) as a function of porosity level is mapped in Figure 13(c). It is observed that S_e increases with the severity of porosity in the part. The ejecta spreads farther as the meltpool becomes instable. The increase in T_e in Figure 13(d) is also associated with the meltpool instability, which leads to ejection of hot meltpool particles during the process (Qiu et al., 2015).

Next, in Figure 14 we test the ability of the four extracted features to differentiate between the three types of porosity and the four porosity levels without the need for a machine learning model. It is noticed that the porosity type (Figure 14(a) and (b)) shows more discernable clustering compared to pore severity (Figure 14(c) and (d)). For example, in Figure 14 (a), while there is significant overlap between lack-of-fusion and conduction (minimal porosity) regimes, a clear separation of features is evident for the keyhole regime. The significant overlap between these clusters and nonlinear interaction between features necessitates the need for machine learning algorithm to predict porosity.

The pore severity and type classification results from the machine learning models, including KNN, SVM, LR, and CNN are shown in Table 5 and pictorially reported in Figure 15. The results indicate that only four features, as porosity predictors in this study, were sufficient to predict the porosity level in LPBF with accuracy exceeding 95% (F1-score) with a simple KNN model.

The false positive rate (FPR, Type I error rate) and false negative rate (FNR, Type II error rate) are both within 3%. This error mainly originates from mislabeling different porosity levels with the high porosity level. This misclassification is particularly associated with the breakdown of meltpool for the high scanning speed condition as a result of Plateau-Rayleigh effect, which in turn results in the high porosity level observed in this work. For example, shown in Figure 16 is the confusion matrix for the 4-way classification of porosity severity using KNN, wherein, the prediction column under high porosity level has values, while all other off-diagonal elements are zero. In other words, the machine learning algorithm erroneously tags nominal to medium-level porosity as belonging to high porosity.

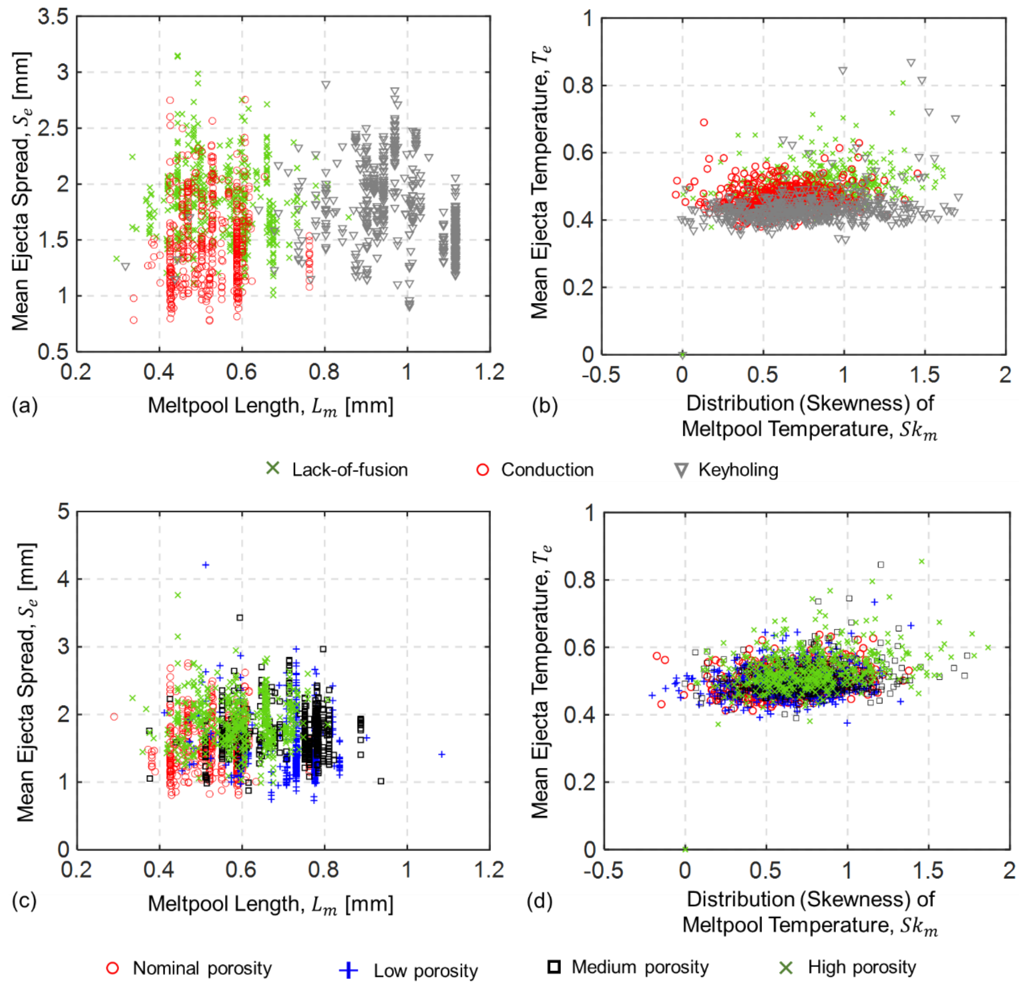

Figure 14: Correlation between features extracted from the dual-wavelength imaging pyrometer frames, where (a) and (b) depict type of porosity, and (c) and (d) depict the severity of porosity.

The results reported in Table 5 are based on the application of the trained machine learning models to the 20% of the unseen data. The logistic regression (LR) model provides the least prediction fidelity of ~70%. The large difference in prediction fidelity of LR and KNN (and SVM) stems from the complex (non-linear) relationship between meltpool signatures and porosity. The SVM model has inferior performance compared to the KNN as it uses a linear function (kernel) to demarcate the nonlinear cluster boundaries depicted in Figure 14. Furthermore, the performance of these physics-informed models was compared with the CNN.

Despite its complex, black-box nature, the CNN did not outperform the KNN model. This is because, CNN models are data hungry and generally require more training data than simpler models (Gaikwad et al., 2020). To explain further, CNN models use the meltpool image data directly without explicitly extracting low-level features. Consequently, a considerably larger number of data points is required by the CNN to capture the natural process variation. Thus, increasing the amount of training data could potentially improve the CNN model results (we exhausted the available data in the current work for training the CNN). Therefore, in Table 5, given its inherently data intensive nature, the performance of the CNN degrades compared to KNN with increasing complexity of the classification task. For example, the F1-score for 2-way pore severity classification the CNN achieves an F1-score of 97%, which decreases to 89% for the 5-way case. To ensure that the models were not trained to the verge of overfitting, learning curve analyses were implemented. Such learning curves are detailed in Appendix B. The results affirm that the number of data points used for training and validating the various models (as reported in Table 3) were appropriate.

Table 5: Results of porosity severity and type classification using different machine learning classifiers in terms of the F1-score, false positive rate (FPR), false negative rate (FNR). The simple machine learning models like KNN perform at par with a black-box CNN.

Porosity classification	Logistic Regression (LR)			Support Vector Machine (SVM)			K-Nearest Neighbors (KNN)			Convolutional Neural Network (CNN)		
	F1-score	FPR	FNR	F1-score	FPR	FNR	F1-score	FPR	FNR	F1-score	FPR	FNR
Task 1 – Classify Type of Porosity (Lack-of-fusion, Conduction, Keyholing)												
3-way	0.83	0.083	0.165	0.85	0.075	0.149	0.97	0.013	0.026	0.94	0.029	0.06
Task 2 – Classify Severity of Porosity												
2-way	0.82	0.185	0.185	0.84	0.159	0.159	0.97	0.030	0.030	0.97	0.034	0.034
3-way	0.74	0.133	0.265	0.77	0.117	0.233	0.98	0.009	0.019	0.95	0.026	0.053
4-way	0.65	0.114	0.341	0.71	0.097	0.029	0.97	0.009	0.027	0.93	0.024	0.072
5-way	0.60	0.101	0.403	0.64	0.090	0.359	0.97	0.013	0.040	0.89	0.028	0.110

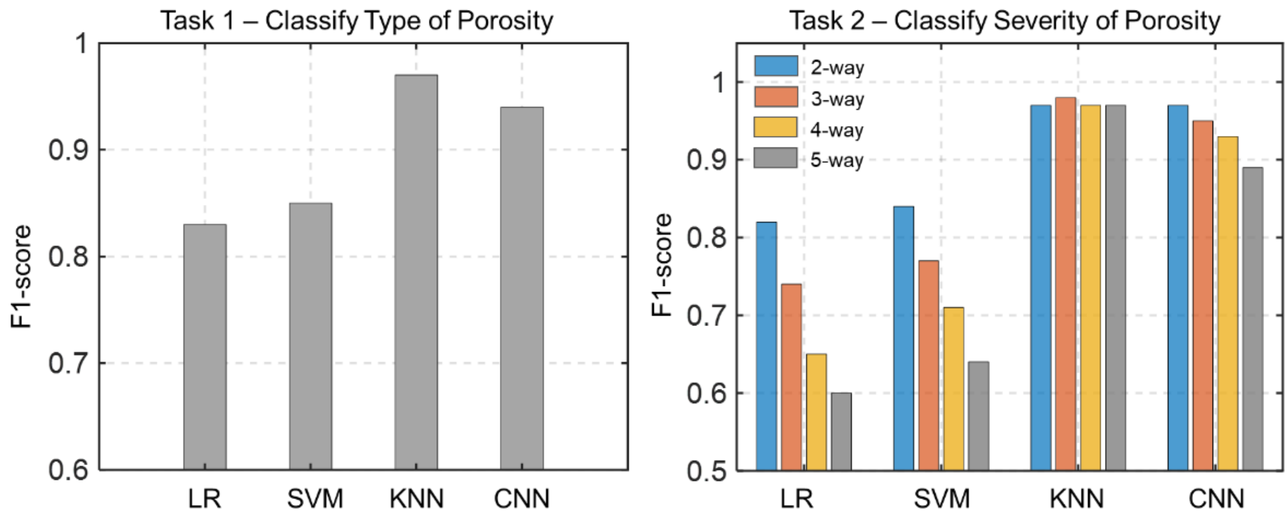

Figure 15: Graphical representation of the porosity type and severity classification using various machine learning models, viz., Logistic Regression (LR), Support Vector Machine (SVM), K-Nearest Neighbors (KNN), Convolutional Neural Network (CNN) in terms of the F1-score. Note the KNN model with physics-informed features performs at par with the CNN which uses the raw meltpool images.

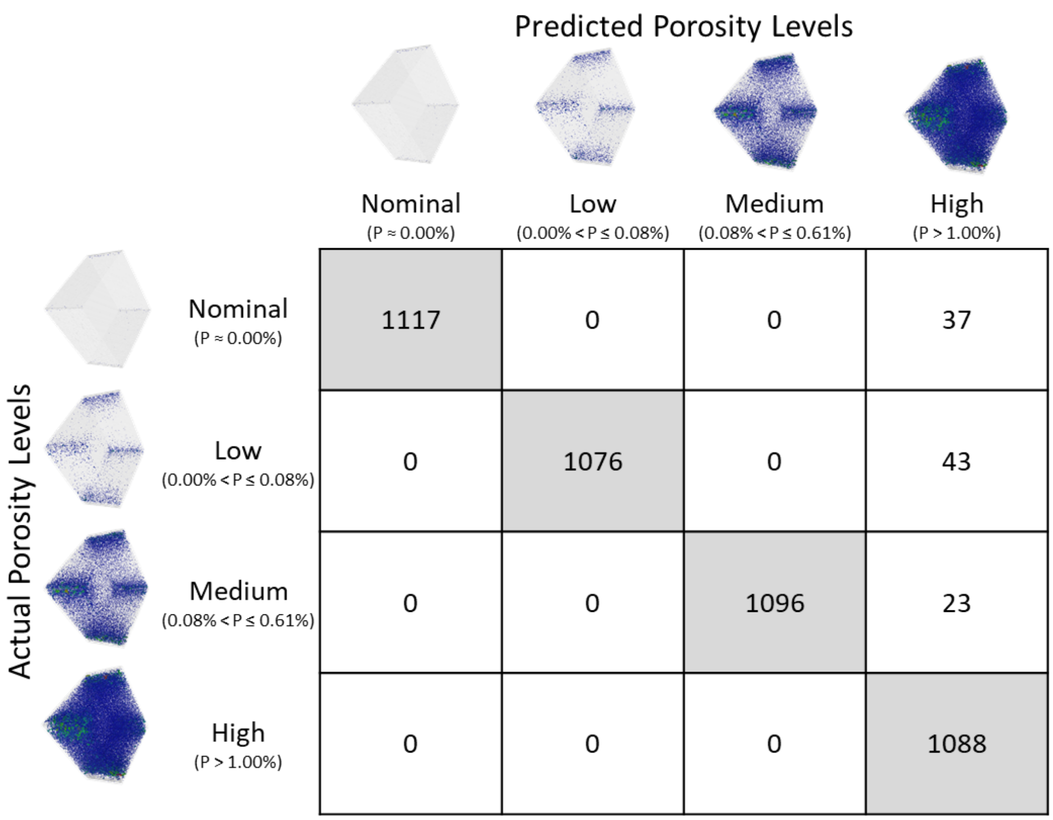

Actual \ Predicted	Nominal	Low	Medium	High
Nominal	1117	0	0	37
Low	0	1076	0	43
Medium	0	0	1096	23
High	0	0	0	1088

Figure 16: Confusion matrix for 4-way classification of porosity severity using K-nearest neighbor (KNN) model. It is noticed that the misclassification error originates from mislabeling different porosity levels with the High porosity level.

4 Conclusion

In this work, we demonstrated the online prediction of flaw formation (porosity) in laser powder bed fusion (LPBF) additive manufacturing process using meltpool signatures acquired from a dual-wavelength pyrometer. The main contribution of this work lies in monitoring and predicting the severity of porosity formation as well as its type based on four physically intuitive meltpool signatures via simple machine learning models. The correlation of meltpool signatures to porosity is achieved through relatively simple and computationally tractable machine learning models, such as K-Nearest Neighbors (KNN) and Support Vector Machine (SVM).

A key finding is that a simple KNN machine learning model performed at par (F1-score > 95%) to a complex black-box deep learning model. The use of easy and interpretable physics-informed process signatures, coupled with readily implementable machine learning, as opposed to black-box deep learning techniques, facilitates rapid detection of flaws, and can therefore eliminate the latency in the data transfer and analysis loop inherent to complex data-driven flaw detection algorithms. In effect, this work takes the first step towards online, real-time flaw detection (qualify-as-you-build) in LPBF.

Specific conclusions from this work are as follows:

(1) A large LPBF part 10 mm × 10 mm × 137 mm (ATI 718Plus) was processed under varying laser power and scanning speed conditions (ten conditions) to engender porosity of different types and varying severity of porosity. A dual wavelength imaging pyrometer was used to continuously monitor the process. The pyrometer acquires meltpool images and temperature maps at a sampling rate of 800 Hz and resolution of 370 × 384 pixels (29 µm per pixel spatial resolution).

(2) The type of porosity in the part was characterized using SEM and optical microscopy. Two types of porosity (lack-of-fusion and keyhole formation) were observed in the sample. The severity of porosity in the part was characterized using non-destructive XCT and Archimedes method. The

XCT analysis revealed that the porosity in the samples ranged from 0 – 2% (defect volume ratio). The corresponding relative density measured from the Archimedes method was 99% – 86%.

(3) Four physically intuitive features were extracted from the meltpool images. These features are based on experimental and theoretical simulation results reported in the literature. Two features capture the shape (morphology) and temperature distribution of the meltpool, and two features capture the temperature and spatial distribution (spread) of the ejecta (spatter).

(4) These meltpool signatures were used as inputs to various types of simple machine learning models, such as Logistic Regression (LR), K-Nearest Neighbors (KNN), Support Vector Machine (SVM) trained to predict the severity and type of porosity. The pore severity and type were classified with a statistical fidelity (F1-score) exceeding 95% with the KNN.

(5) The results obtained from the KNN were comparable to those from deep learning convolutional neural network (CNN) that uses raw meltpool images instead of meltpool features.

In the future, we will endeavor to extend our studies to complex geometries and different materials to test for transferability of the proposed approach.

Acknowledgements

The experiments and data acquired for this work was funded by Defense Advanced Research Projects Agency (DARPA) Defense Sciences Office (DSO) under contract HR00110120C-0037 *Rapid Low Cost Additive Manufacturing* (Program Officers: Mick Maher and Jan Vandenbrande).

Prahalada Rao thanks the National Science Foundation (NSF) and Department of Energy (DoE) for funding his work under awards OIA-1929172, CMMI-1920245, CMMI-1739696, ECCS-2020246, PFI-TT 2044710, CMMI-1752069, CMMI-1719388, and DE-SC0021136. Understanding the causal influence of process parameters on part quality and detection of defect formation using in-situ sensing was the major aspect of CMMI-1752069 (Program Officer: Kevin Chou). The use of AI algorithms for defect detection in additive manufacturing was proposed in ECCS-2020246 (Program Officer: Donald Wunsch). Supplemental funding for CMMI-1752069 was obtained through the NSF INTERN program (Program Officer: Prakash Balan) and CMMI Data Science Activities (Program Officer: Martha Dodson) is greatly appreciated. The latter supplement funded Ziyad Smoqi and Aniruddha Gaikwad's research. The X-ray CT analysis was conducted on the instrument partially funded through the Major Research Instrumentation grant (CMMI-1920245, program officer: Wendy C. Crone). Ben Bevans' work was funded partially through the DoE Grant DE-SC0021136. The materials characterization research was performed in part in the Nebraska Nanoscale Facility: National Nanotechnology Coordinated Infrastructure under award no. ECCS: 2025298, and with support from the Nebraska Research Initiative through the Nebraska Center for Materials and Nanoscience and the Nanoengineering Research Core Facility at the University of Nebraska-Lincoln.

References

Ali, U., Esmaeilizadeh, R., Ahmed, F., Sarker, D., Muhammad, W., Keshavarzkermani, A., Mahmoodkhani, Y., Marzbanrad, E., Toyserkani, E., 2019. Identification and characterization of spatter particles and their effect on surface roughness, density and mechanical response of 17-4 PH stainless steel laser powder-bed fusion parts. Materials Science and Engineering: A 756, 98-107. https://doi.org/10.1016/j.msea.2019.04.026

Clijsters, S., Craeghs, T., Buls, S., Kempen, K., Kruth, J.P., 2014. In situ quality control of the selective laser melting process using a high-speed, real-time melt pool monitoring system. The International Journal of Advanced Manufacturing Technology 75, 1089-1101. https://doi.org/10.1007/s00170-014-6214-8

Darvish, K., Chen, Z.W., Pasang, T., 2016. Reducing lack of fusion during selective laser melting of CoCrMo alloy: Effect of laser power on geometrical features of tracks. Materials & Design 112, 357-366. https://doi.org/10.1016/j.matdes.2016.09.086

DebRoy, T., Wei, H.L., Zuback, J.S., Mukherjee, T., Elmer, J.W., Milewski, J.O., Beese, A.M., Wilson-Heid, A., De, A., Zhang, W., 2018. Additive manufacturing of metallic components – Process, structure and properties. Progress in Materials Science 92, 112-224. https://doi.org/10.1016/j.pmatsci.2017.10.001

Diehl, B., Nassar, A., 2020. Reducing near-surface voids in metal (Ti-6Al-4V) powder bed fusion additive manufacturing: the effect of inter-hatch travel time. Additive Manufacturing 36, 101592. https://doi.org/10.1016/j.addma.2020.101592

Druzgalski, C.L., Ashby, A., Guss, G., King, W.E., Roehling, T.T., Matthews, M.J., 2020. Process optimization of complex geometries using feed forward control for laser powder bed fusion additive manufacturing. Additive Manufacturing 34, 101169. https://doi.org/10.1016/j.addma.2020.101169

du Plessis, A., 2019. Effects of process parameters on porosity in laser powder bed fusion revealed by X-ray tomography. Additive Manufacturing 30, 100871. https://doi.org/10.1016/j.addma.2019.100871

Du, Y., Mukherjee, T., DebRoy, T., 2021. Physics-informed machine learning and mechanistic modeling of additive manufacturing to reduce defects. Applied Materials Today 24, 101123. https://doi.org/10.1016/j.apmt.2021.101123

Esmaeilizadeh, R., Ali, U., Keshavarzkermani, A., Mahmoodkhani, Y., Marzbanrad, E., Toyserkani, E., 2019. On the effect of spatter particles distribution on the quality of Hastelloy X parts made by laser powder-bed fusion additive manufacturing. Journal of Manufacturing Processes 37, 11-20. https://doi.org/10.1016/j.jmapro.2018.11.012

Everton, S.K., Hirsch, M., Stravroulakis, P., Leach, R.K., Clare, A.T., 2016. Review of in-situ process monitoring and in-situ metrology for metal additive manufacturing. Materials & Design 95, 431-445. https://doi.org/10.1016/j.matdes.2016.01.099

Fedina, T., Sundqvist, J., Kaplan, A.F.H., 2021. Spattering and oxidation phenomena during recycling of low alloy steel powder in Laser Powder Bed Fusion. Materials Today Communications 27, 102241. https://doi.org/10.1016/j.mtcomm.2021.102241

Felix, S., Majumder, S.R., Mathews, H.K., Lexa, M., Lipsa, G., Ping, X., Roychowdhury, S., Spears, T., 2021. In situ process quality monitoring and defect detection for direct metal laser melting. arXiv preprint arXiv:2112.01921.

Forien, J.-B., Calta, N.P., DePond, P.J., Guss, G.M., Roehling, T.T., Matthews, M.J., 2020. Detecting keyhole pore defects and monitoring process signatures during laser powder bed fusion: A correlation between in situ pyrometry and ex situ X-ray radiography. Additive Manufacturing 35, 101336. https://doi.org/10.1016/j.addma.2020.101336

Foster, B., Reutzel, E., Nassar, A., Hall, B., Brown, S., Dickman, C., 2015. Optical, layerwise monitoring of powder bed fusion, Solid Freeform Fabrication Symposium, Austin, TX, Aug, pp. 10-12.

Gaikwad, A., Giera, B., Guss, G.M., Forien, J.-B., Matthews, M.J., Rao, P., 2020. Heterogeneous sensing and scientific machine learning for quality assurance in laser powder bed fusion – A single-track study. Additive Manufacturing 36, 101659. https://doi.org/10.1016/j.addma.2020.101659

Gaikwad, A., Imani, F., Yang, H., Reutzel, E., Rao, P., 2019. In Situ Monitoring of Thin-Wall Build Quality in Laser Powder Bed Fusion Using Deep Learning. Smart and Sustainable Manufacturing Systems 3. SSMS 2019 0027.R2

Gibson, I., Rosen, D.W., Stucker, B., Khorasani, M., 2021. Additive manufacturing technologies. Springer.

Giovagnoli, M., Silvi, G., Merlin, M., Di Giovanni, M.T., 2021. Optimisation of process parameters for an additively manufactured AlSi10Mg alloy: Limitations of the energy density-based approach on porosity and mechanical properties estimation. Materials Science and Engineering: A 802, 140613. https://doi.org/10.1016/j.msea.2020.140613

Gorelik, M., 2017. Additive manufacturing in the context of structural integrity. International Journal of Fatigue 94, 168-177. https://doi.org/10.1016/j.ijfatigue.2016.07.005

Grasso, M., Colosimo, B.M., 2017. Process defects and in situ monitoring methods in metal powder bed fusion: a review. Meas. Sci. Technol. 28, 044005. https://doi.org/10.1088/1361-6501/aa5c4f

Grasso, M., Colosimo, B.M., 2019. A statistical learning method for image-based monitoring of the plume signature in laser powder bed fusion. Robotics and Computer-Integrated Manufacturing 57, 103-115. https://doi.org/10.1016/j.rcim.2018.11.007

Guo, C., Li, S., Shi, S., Li, X., Hu, X., Zhu, Q., Ward, R.M., 2020. Effect of processing parameters on surface roughness, porosity and cracking of as-built IN738LC parts fabricated by laser powder bed fusion. Journal of Materials Processing Technology 285, 116788. https://doi.org/10.1016/j.jmatprotec.2020.116788

Guo, Q., Zhao, C., Qu, M., Xiong, L., Escano, L.I., Hojjatzadeh, S.M.H., Parab, N.D., Fezzaa, K., Everhart, W., Sun, T., Chen, L., 2019. In-situ characterization and quantification of melt pool variation under constant input energy density in laser powder bed fusion additive manufacturing process. Additive Manufacturing 28, 600-609. https://doi.org/10.1016/j.addma.2019.04.021

Guo, S., Agarwal, M., Cooper, C., Tian, Q., Gao, R.X., Guo, W., Guo, Y.B., 2022. Machine learning for metal additive manufacturing: Towards a physics-informed data-driven paradigm. Journal of Manufacturing Systems 62, 145-163. https://doi.org/10.1016/j.jmsy.2021.11.003

Heigel, J.C., Lane, B.M., 2018. Measurement of the melt pool length during single scan tracks in a commercial laser powder bed fusion process. Journal of Manufacturing Science and Engineering 140. https://doi.org/10.1115/1.4037571

Hooper, P.A., 2018. Melt pool temperature and cooling rates in laser powder bed fusion. Additive Manufacturing 22, 548-559. https://doi.org/10.1016/j.addma.2018.05.032

Kamath, C., El-dasher, B., Gallegos, G.F., King, W.E., Sisto, A., 2014. Density of additively-manufactured, 316L SS parts using laser powder-bed fusion at powers up to 400 W. The International Journal of Advanced Manufacturing Technology 74, 65-78. 10.1007/s00170-014-5954-9

Kasperovich, G., Haubrich, J., Gussone, J., Requena, G., 2016. Correlation between porosity and processing parameters in TiAl6V4 produced by selective laser melting. Materials & Design 105, 160-170. https://doi.org/10.1016/j.matdes.2016.05.070

Kennedy, R., 2005. ALLVAC® 718PLUS™, superalloy for the next forty years. The Minerals, Metals & Materials Society, 1-14.

Khairallah, S.A., Anderson, A.T., Rubenchik, A., King, W.E., 2016. Laser powder-bed fusion additive manufacturing: Physics of complex melt flow and formation mechanisms of pores, spatter, and denudation zones. Acta Materialia 108, 36-45. https://doi.org/10.1016/j.actamat.2016.02.014

King, W., Anderson, A.T., Ferencz, R.M., Hodge, N.E., Kamath, C., Khairallah, S.A., 2015. Overview of modelling and simulation of metal powder bed fusion process at Lawrence Livermore National Laboratory. Materials Science and Technology 31, 957-968. https://doi.org/10.1179/1743284714Y.0000000728

King, W.E., Barth, H.D., Castillo, V.M., Gallegos, G.F., Gibbs, J.W., Hahn, D.E., Kamath, C., Rubenchik, A.M., 2014. Observation of keyhole-mode laser melting in laser powder-bed fusion additive manufacturing. Journal of Materials Processing Technology 214, 2915-2925. https://doi.org/10.1016/j.jmatprotec.2014.06.005

Kingma, D.P., Ba, J., 2014. Adam: A method for stochastic optimization. arXiv preprint arXiv:1412.6980.

Kwon, O., Kim, H.G., Ham, M.J., Kim, W., Kim, G.-H., Cho, J.-H., Kim, N.I., Kim, K., 2020. A deep neural network for classification of melt-pool images in metal additive manufacturing. Journal of Intelligent Manufacturing 31, 375-386. https://doi.org/10.1007/s10845-018-1451-6

Lane, B., Heigel, J., Ricker, R., Zhirnov, I., Khromschenko, V., Weaver, J., Phan, T., Stoudt, M., Mekhontsev, S., Levine, L., 2020a. Measurements of Melt Pool Geometry and Cooling Rates of Individual Laser Traces on IN625 Bare Plates. Integrating Materials and Manufacturing Innovation 9, 16-30. https://doi.org/10.1007/s40192-020-00169-1

Lane, B., Jacquemetton, L., Piltch, M., Beckett, D., 2020b. Thermal Calibration of Commercial Melt Pool Monitoring Sensors on a Laser Powder Bed Fusion System. National Institute of Standards and

Technology (NIST), Advanced Manufacturing Series. Series 100-35. https://doi.org/10.6028/NIST.AMS.100-35

Lewandowski, J.J., Seifi, M., 2016. Metal Additive Manufacturing: A Review of Mechanical Properties. Annual Review of Materials Research 46, 151-186. https://doi.org/10.1146/annurev-matsci-070115-032024

Li, E.L., Wang, L., Yu, A.B., Zhou, Z.Y., 2021. A three-phase model for simulation of heat transfer and melt pool behaviour in laser powder bed fusion process. Powder Technology 381, 298-312. https://doi.org/10.1016/j.powtec.2020.11.061

Li, J., Cao, L., Xu, J., Wang, S., Zhou, Q., 2022. In situ porosity intelligent classification of selective laser melting based on coaxial monitoring and image processing. Measurement 187, 110232. https://doi.org/10.1016/j.measurement.2021.110232

Ly, S., Rubenchik, A.M., Khairallah, S.A., Guss, G., Matthews, M.J., 2017. Metal vapor micro-jet controls material redistribution in laser powder bed fusion additive manufacturing. Scientific Reports 7, 4085. https://doi.org/10.1038/s41598-017-04237-z

Mani, M., Lane, B.M., Donmez, M.A., Feng, S.C., Moylan, S.P., 2017. A review on measurement science needs for real-time control of additive manufacturing metal powder bed fusion processes. International Journal of Production Research 55, 1400-1418. https://doi.org/10.1080/00207543.2016.1223378

Megahed, M., Mindt, H.-W., Willems, J., Dionne, P., Jacquemetton, L., Craig, J., Ranade, P., Peralta, A., 2019. LPBF Right the First Time—the Right Mix Between Modeling and Experiments. Integrating Materials and Manufacturing Innovation 8, 194-216. https://doi.org/10.1007/s40192-019-00133-8

Meng, L., McWilliams, B., Jarosinski, W., Park, H.-Y., Jung, Y.-G., Lee, J., Zhang, J., 2020. Machine Learning in Additive Manufacturing: A Review. JOM 72, 2363-2377. https://doi.org/10.1007/s11837-020-04155-y

Mitchell, J.A., Ivanoff, T.A., Dagel, D., Madison, J.D., Jared, B., 2020. Linking pyrometry to porosity in additively manufactured metals. Additive Manufacturing 31, 100946. https://doi.org/10.1016/j.addma.2019.100946

Montazeri, M., Nassar, A.R., Dunbar, A.J., Rao, P., 2020. In-process monitoring of porosity in additive manufacturing using optical emission spectroscopy. IISE Transactions 52, 500-515. https://doi.org/10.1080/24725854.2019.1659525

Moylan, S., Whitenton, E., Lane, B., Slotwinski, J., 2014. Infrared thermography for laser-based powder bed fusion additive manufacturing processes. AIP Conference Proceedings 1581, 1191-1196. https://doi.org/10.1063/1.4864956

Mozaffar, M., Liao, S., Xie, X., Saha, S., Park, C., Cao, J., Liu, W.K., Gan, Z., 2022. Mechanistic artificial intelligence (mechanistic-AI) for modeling, design, and control of advanced manufacturing processes: Current state and perspectives. Journal of Materials Processing Technology 302, 117485. https://doi.org/10.1016/j.jmatprotec.2021.117485

Mucherino, A., Papajorgji, P.J., Pardalos, P.M., 2009. k-Nearest Neighbor Classification, In: Mucherino, A., Papajorgji, P.J., Pardalos, P.M. (Eds.), Data Mining in Agriculture. Springer New York, New York, NY, pp. 83-106.

Nassar, A.R., Gundermann, M.A., Reutzel, E.W., Guerrier, P., Krane, M.H., Weldon, M.J., 2019. Formation processes for large ejecta and interactions with melt pool formation in powder bed fusion additive manufacturing. Scientific Reports 9, 5038. https://doi.org/10.1038/s41598-019-41415-7

Ness, K.L., Paul, A., Sun, L., Zhang, Z., 2022. Towards a generic physics-based machine learning model for geometry invariant thermal history prediction in additive manufacturing. Journal of Materials Processing Technology 302, 117472. https://doi.org/10.1016/j.jmatprotec.2021.117472

Oliveira, J.P., LaLonde, A.D., Ma, J., 2020a. Processing parameters in laser powder bed fusion metal additive manufacturing. Materials & Design 193, 108762. https://doi.org/10.1016/j.matdes.2020.108762

Oliveira, J.P., Santos, T.G., Miranda, R.M., 2020b. Revisiting fundamental welding concepts to improve additive manufacturing: From theory to practice. Progress in Materials Science 107, 100590. https://doi.org/10.1016/j.pmatsci.2019.100590

Pantawane, M.V., Ho, Y.-H., Joshi, S.S., Dahotre, N.B., 2020. Computational Assessment of Thermokinetics and Associated Microstructural Evolution in Laser Powder Bed Fusion Manufacturing of Ti6Al4V Alloy. Scientific Reports 10, 7579. https://doi.org/10.1038/s41598-020-63281-4

Qiu, C., Panwisawas, C., Ward, M., Basoalto, H.C., Brooks, J.W., Attallah, M.M., 2015. On the role of melt flow into the surface structure and porosity development during selective laser melting. Acta Materialia 96, 72-79. https://doi.org/10.1016/j.actamat.2015.06.004

Ramalho, A., Santos, T.G., Bevans, B., Smoqi, Z., Rao, P., Oliveira, J.P., 2022. Effect of contaminations on the acoustic emissions during wire and arc additive manufacturing of 316L stainless steel. Additive Manufacturing 51, 102585. https://doi.org/10.1016/j.addma.2021.102585

Rankouhi, B., Agrawal, A.K., Pfefferkorn, F.E., Thoma, D.J., 2021. A dimensionless number for predicting universal processing parameter boundaries in metal powder bed additive manufacturing. Manufacturing Letters 27, 13-17. https://doi.org/10.1016/j.mfglet.2020.12.002

Razvi, S.S., Feng, S., Narayanan, A., Lee, Y.-T.T., Witherell, P., 2019. A Review of Machine Learning Applications in Additive Manufacturing, ASME 2019 International Design Engineering Technical Conferences and Computers and Information in Engineering Conference.

Repossini, G., Laguzza, V., Grasso, M., Colosimo, B.M., 2017. On the use of spatter signature for in-situ monitoring of Laser Powder Bed Fusion. Additive Manufacturing 16, 35-48. https://doi.org/10.1016/j.addma.2017.05.004

Romano, J., Ladani, L., Razmi, J., Sadowski, M., 2015. Temperature distribution and melt geometry in laser and electron-beam melting processes – A comparison among common materials. Additive Manufacturing 8, 1-11. https://doi.org/10.1016/j.addma.2015.07.003

Ronneberg, T., Davies, C.M., Hooper, P.A., 2020. Revealing relationships between porosity, microstructure and mechanical properties of laser powder bed fusion 316L stainless steel through heat treatment. Materials & Design 189, 108481. https://doi.org/10.1016/j.matdes.2020.108481

Sames, W.J., List, F.A., Pannala, S., Dehoff, R.R., Babu, S.S., 2016. The metallurgy and processing science of metal additive manufacturing. International Materials Reviews 61, 315-360. https://doi.org/10.1080/09506608.2015.1116649

Schwerz, C., Raza, A., Lei, X., Nyborg, L., Hryha, E., Wirdelius, H., 2021. In-situ detection of redeposited spatter and its influence on the formation of internal flaws in laser powder bed fusion. Additive Manufacturing 47, 102370. https://doi.org/10.1016/j.addma.2021.102370

Scime, L., Beuth, J., 2019. Using machine learning to identify in-situ melt pool signatures indicative of flaw formation in a laser powder bed fusion additive manufacturing process. Additive Manufacturing 25, 151-165. https://doi.org/10.1016/j.addma.2018.11.010

Scipioni Bertoli, U., Wolfer, A.J., Matthews, M.J., Delplanque, J.-P.R., Schoenung, J.M., 2017. On the limitations of Volumetric Energy Density as a design parameter for Selective Laser Melting. Materials & Design 113, 331-340. https://doi.org/10.1016/j.matdes.2016.10.037

Seifi, M., Salem, A., Beuth, J., Harrysson, O., Lewandowski, J.J., 2016. Overview of materials qualification needs for metal additive manufacturing. Jom 68, 747-764. https://doi.org/10.1007/s11837-015-1810-0

Slotwinski, J.A., Garboczi, E.J., 2014. Porosity of additive manufacturing parts for process monitoring, AIP conference proceedings. American Institute of Physics, pp. 1197-1204.

Snow, Z., Diehl, B., Reutzel, E.W., Nassar, A., 2021. Toward in-situ flaw detection in laser powder bed fusion additive manufacturing through layerwise imagery and machine learning. Journal of Manufacturing Systems 59, 12-26. https://doi.org/10.1016/j.jmsy.2021.01.008

Snow, Z., Nassar, A.R., Reutzel, E.W., 2020. Invited Review Article: Review of the formation and impact of flaws in powder bed fusion additive manufacturing. Additive Manufacturing 36, 101457. https://doi.org/10.1016/j.addma.2020.101457

Snow, Z., Reutzel, E.W., Petrich, J., 2022. Correlating in-situ sensor data to defect locations and part quality for additively manufactured parts using machine learning. Journal of Materials Processing Technology 302, 117476. https://doi.org/10.1016/j.jmatprotec.2021.117476

Spears, T.G., Gold, S.A., 2016. In-process sensing in selective laser melting (SLM) additive manufacturing. Integrating Materials and Manufacturing Innovation 5, 16-40. https://doi.org/10.1186/s40192-016-0045-4

Tan, Z., Fang, Q., Li, H., Liu, S., Zhu, W., Yang, D., 2020. Neural network based image segmentation for spatter extraction during laser-based powder bed fusion processing. Optics & Laser Technology 130, 106347. https://doi.org/10.1016/j.optlastec.2020.106347

Tang, M., Pistorius, P.C., Beuth, J.L., 2017. Prediction of lack-of-fusion porosity for powder bed fusion. Additive Manufacturing 14, 39-48. https://doi.org/10.1016/j.addma.2016.12.001

Wang, C., Tan, X.P., Tor, S.B., Lim, C.S., 2020. Machine learning in additive manufacturing: State-of-the-art and perspectives. Additive Manufacturing 36, 101538. https://doi.org/10.1016/j.addma.2020.101538

Wardhani, N.W.S., Rochayani, M.Y., Iriany, A., Sulistyono, A.D., Lestantyo, P., 2019. Cross-validation Metrics for Evaluating Classification Performance on Imbalanced Data, 2019 International Conference on Computer, Control, Informatics and its Applications (IC3INA), pp. 14-18.

Wells, J.M., 2007. Quantitative XCT evaluation of porosity in an aluminum alloy casting, Shape casting: 2nd international symposium, pp. 978-970.

Yadollahi, A., Shamsaei, N., 2017. Additive manufacturing of fatigue resistant materials: Challenges and opportunities. International Journal of Fatigue 98, 14-31. https://doi.org/10.1016/j.ijfatigue.2017.01.001

Yavari, R., Riensche, A., Tekerek, E., Jacquemetton, L., Halliday, H., Vandever, M., Tenequer, A., Perumal, V., Kontsos, A., Smoqi, Z., Cole, K., Rao, P., 2021a. Digitally twinned additive manufacturing: Detecting flaws in laser powder bed fusion by combining thermal simulations with in-situ meltpool sensor data. Materials & Design 211, 110167. https://doi.org/10.1016/j.matdes.2021.110167

Yavari, R., Smoqi, Z., Riensche, A., Bevans, B., Kobir, H., Mendoza, H., Song, H., Cole, K., Rao, P., 2021b. Part-scale thermal simulation of laser powder bed fusion using graph theory: Effect of thermal history on porosity, microstructure evolution, and recoater crash. Materials & Design 204, 109685. https://doi.org/10.1016/j.matdes.2021.109685

Ye, D., Hsi Fuh, J.Y., Zhang, Y., Hong, G.S., Zhu, K., 2018. In situ monitoring of selective laser melting using plume and spatter signatures by deep belief networks. ISA Transactions 81, 96-104. https://doi.org/10.1016/j.isatra.2018.07.021

Zhang, Y., Hong, G.S., Ye, D., Zhu, K., Fuh, J.Y.H., 2018. Extraction and evaluation of melt pool, plume and spatter information for powder-bed fusion AM process monitoring. Materials & Design 156, 458-469. https://doi.org/10.1016/j.matdes.2018.07.002

Appendix A: Convolutional Neural Network (CNN)

A deep convolutional neural network (CNN) was used to classify the severity and type of porosity using the meltpool images acquired from the dual-wavelength pyrometer. The meltpool images were centered and rotated before using them as inputs to the CNN as shown in Figure A1. Subsequently, the images were cropped to a dimension of 200 × 200 pixels to reduce the computational burden while training the CNN.

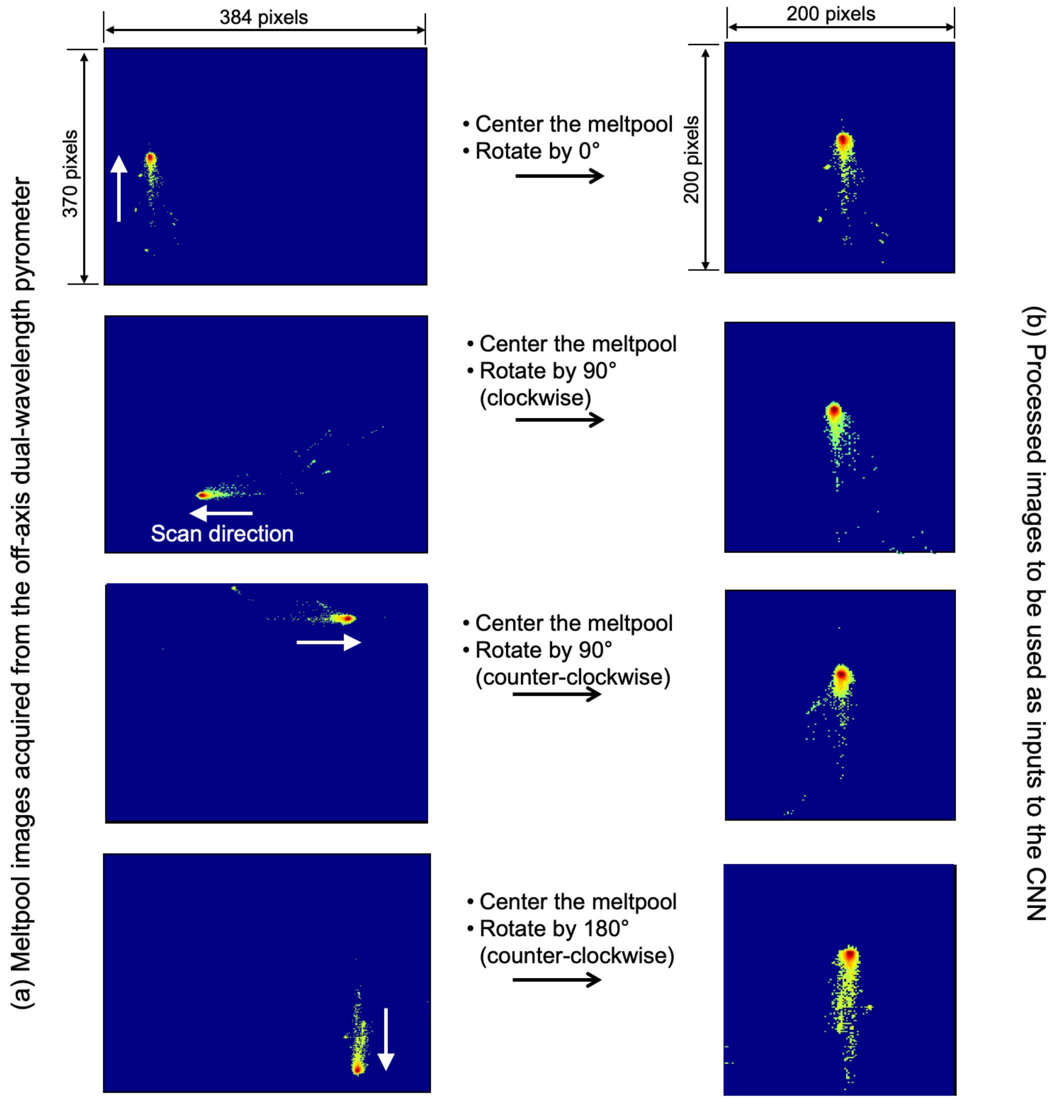

Figure A1: Image preprocessing for Convolutional Neural Network (CNN). (a) Representative meltpool images acquired from the dual-wavelength pyrometer. (b) Centered and reoriented meltpool images.

Figure A2 elucidates the architecture of the CNN used in this work. The first layer is the input layer which uses the rotated and centered meltpool images. This is followed by four blocks, with each block consisting of convolutional layers, batch normalization layer, and max pooling layers (L2-regularization was used in the convolutional layers to avoid overfitting). Similarly, the last block has a dropout layer to further avoid overfitting of the model while training. The CNN was trained using the adaptive learning optimization with the help of the Adam solver (Kingma and Ba, 2014). The convolutional layers and fully connected layers use ReLU (Rectified Linear Unit) activation function to introduce nonlinearity. The size of the output layer depends on the classification task. For example, for the 4-way pore severity classification the output layer has 4 neurons.

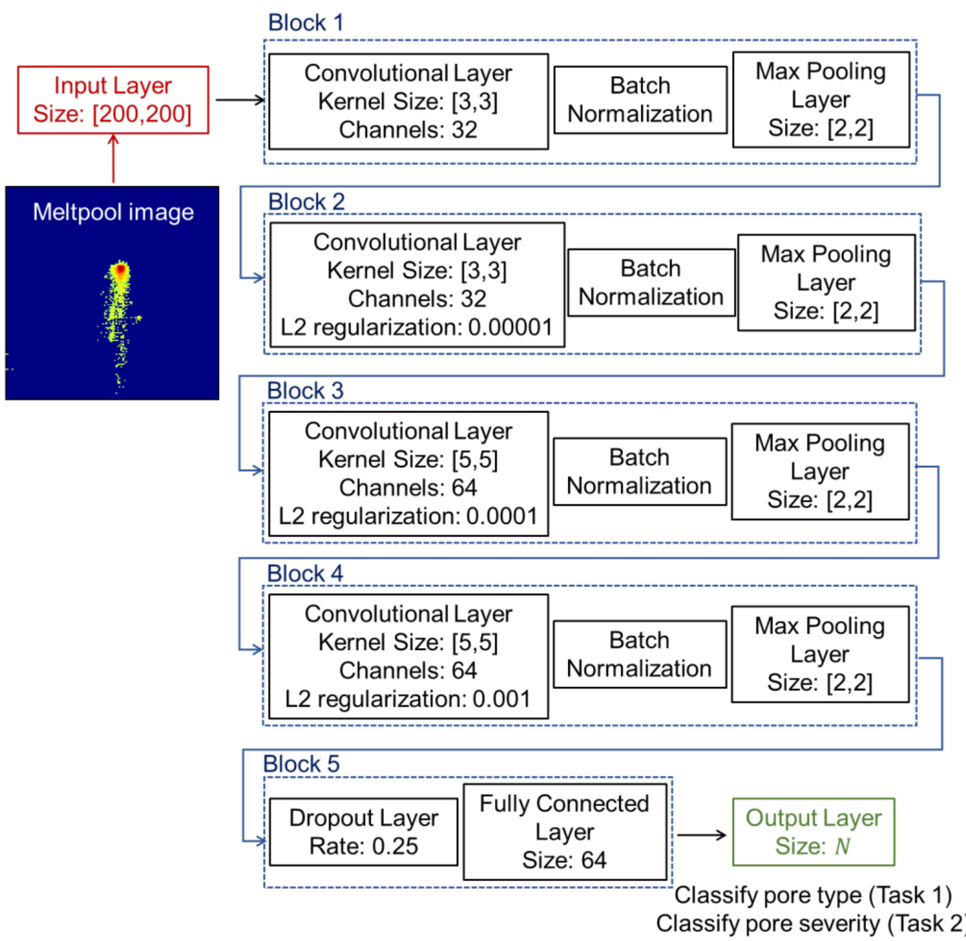

Figure A2: Schematic of the Convolutional Neural Network's (CNN) architecture. Preprocessed meltpool images (Figure A1) were used as inputs to the CNN. The size of the output layer (N) depends on the complexity of the classification task.

Appendix B: Learning Curves for K-Nearest Neighbors (KNN)

To estimate the minimum data required to train the machine learning modes, a learning curve was generated for each of the prediction cases using its original set of data. The various models were trained on increasing increments of 100 datapoints, using 80% of the data. Then, the trained model was validated on an independent test data (20%) after each run. Figure A3 shows the learning curves for the KNN model with respect to 2-, 3-, and 4-way classification of pore severity and 3-way classification of pore type. From the Figures A3, we observe that the minimum number of datapoints required for training lies between 4,000 and 7,000, depending on the complexity of the machine learning task.

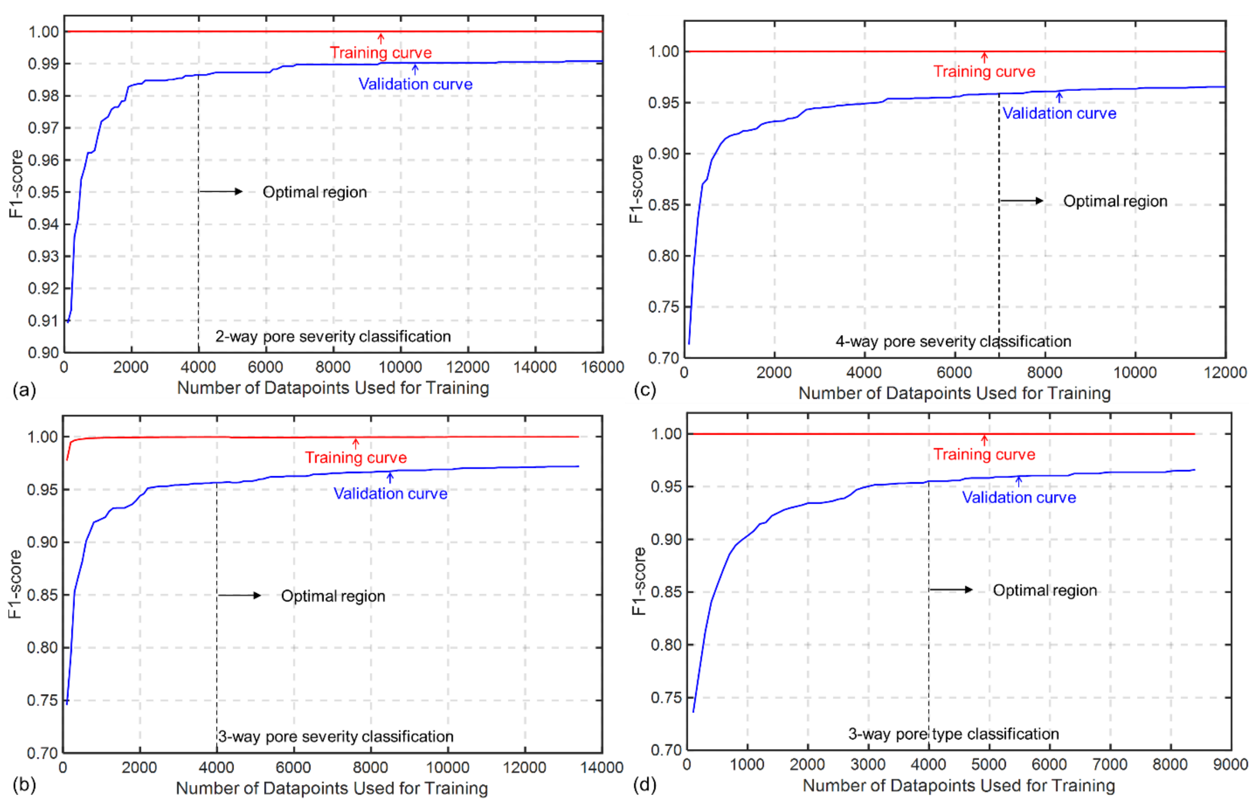

Figure A3: Learning curves for the KNN model used to classify porosity based on the level of pore severity (a – c), and pore type (d). The minimum number of datapoints required to train the model to result in a stable F1-score is estimated to be between 4,000 and 7,000 datapoints.